EFFECT OF INITIAL CONDITIONS ON THE DEVELOPMENT OF RAYLEIGH-TAYLOR INSTABILITIES

A Thesis

by

FREEMAN MICHAEL PEART

Submitted to the Office of Graduate Studies of
Texas A&M University
in partial fulfillment of the requirements for the degree of

MASTER OF SCIENCE

August 2008

Major Subject: Mechanical Engineering

EFFECT OF INITIAL CONDITIONS ON THE DEVELOPMENT OF RAYLEIGH-TAYLOR INSTABILITIES

A Thesis

by

FREEMAN MICHAEL PEART

Submitted to the Office of Graduate Studies of
Texas A&M University
in partial fulfillment of the requirements for the degree of

MASTER OF SCIENCE

Approved by:

Chair of Committee,	Malcolm J. Andrews
Committee Members,	Timothy Jacobs
	Adonios Karpetis
Head of Department,	Dennis O'Neal

August 2008

Major Subject: Mechanical Engineering

ABSTRACT

Effect of Initial Conditions on the Development of

Rayleigh-Taylor Instabilities.

(August 2008)

Freeman Michael Peart, B.S., Texas A&M University

Chair of Advisory Committee: Dr. Malcolm J. Andrews

There are two coupled objectives for this study of buoyancy-driven turbulence. The first objective is to determine if the development of a Rayleigh-Taylor (RT) mixing layer can be manipulated experimentally by altering the initial condition of the experiment. The second objective is to evaluate the performance of the Besnard, Harlow, and Rauenzahn (BHR) turbulent transport model when initialized with experimentally measured initial conditions. An existing statistically steady water channel facility at Texas A&M University and existing experimental diagnostics developed for this facility have been used to measure the turbulent quantities of buoyancy-driven turbulence. A stationary, bi-planar grid with a high solidity ratio, σ, has been placed immediately downstream of the termination of the splitter plate, perpendicular to the flow direction, to generate a turbulent initial condition. The self-similar growth parameter, α, for the RT mixing layer has been measured using a visualization technique to determine if the initial conditions affect the development of the RT mixing layer. The self-similar growth parameter, α, decreased from a value of 0.072 ± 0.0003 with the fine grid to values of 0.063 ± 0.0003 and 0.060 ± 0.0003 with the medium and coarse grids, respectively. With the results from the first objective, a unique opportunity arose to evaluate the performance of the variable density, RANS-type, BHR turbulent transport model. Measurements of velocity statistics

necessary to initialize the model accurately have been obtained using particle image velocimetry (PIV). The performance of the BHR model was evaluated through comparison of the experimentally measured and BHR modeled self-similar growth parameter, α, from the penetration height of the bubbles/spikes and the self-similar growth parameter, α_K, of the turbulent kinetic energy at the centerline of the low Atwood RT driven turbulent mixing layer. When initialized with the experimentally measured initial conditions, the BHR model did agree with the experimental measurements of the penetration height growth parameter, α, as well as the centerline turbulent kinetic energy growth parameter, α_K, in the self-similar portion of the flow.

ACKNOWLEDGEMENTS

I would like to thank my advisor, Dr. Malcolm Andrews, and the sponsor of the research, Dr. Robert Gore, for their patience and guidance throughout the course of this research. I would also like to thank my former co-workers, especially Dr. Wayne Kraft, Dr. Nicholas Meuschke and Dr. Arindam Banerjee, for their assistance and support in the completion of this work. Finally, I would like to thank my friends and family for their encouragement and support, and especially my wife, Rachael, for being so loving and patient with me.

NOMENCLATURE

A	Decay coefficient based on initial conditions of the flow
A_t	Atwood number $\left[\equiv(\rho_l - \rho_h)/(\rho_l + \rho_h)\right]$
a	BHR model parameter for turbulent mass flux
α	Self-similar growth parameter for the penetration height of the bubbles/spikes in a low-Atwood RT mixiang layer
α_K	Self-similar growth parameter for the turbulent kinetic energy in a RT mixing layer
$C2$	Isotropic decay constant for the BHR model
$C4$	Weighting constant for the turbulent length scale equation for the BHR model
d	Rod diameter (cm)
ε	Dissipation (cm^2/s^3)
$\overline{f_V}$	Mixture fraction of the heavy (cold) fluid
g	Gravitational acceleration (cm/s^2)
H	Height of the flow domain (cm)
h	Penetration height of the bubbles/spikes of the low-Atwood RT mix layer (cm)
I_o, I_{min}, I_{max}, I_{corr}	Light intensities of the light source, minimum measured, maximum measured and corrected light intensities from the image
$\overline{K_{GT}}$	Turbulent kinetic energy of the grid-generated turbulence (i.e. outside the RT mixing layer) (cm^2/s^2)
$\overline{K_{RT}}$	Turbulent kinetic energy at the centerline of the RT mixing layer (cm^2/s^2)
κ	Monochromatic extinction coefficient

M	Grid spacing (cm)
n	Isotropic decay exponent for grid-generated turbulence
ν	Kinematic viscosity (cm^2/s)
Re_M	Grid Reynolds number
ρ_h, ρ_l	Density of the heavy (cold) and light (warm) fluid (kg/cm^3)
$\overline{S}$	Turbulent length scale (cm)
σ	Grid solidity ratio
t	Time (s)
τ	Non-dimensional time
U_m	Mean advective velocity for the water channel (cm/s)
u', v', w'	Stream-wise, vertical, and span-wise velocity fluctuations (cm/s)
ω	Absolute extinction coefficient
X, Y, Z	Laboratory coordinates for the stream-wise, vertical, and span-wise directions
x	Distance downstream from the termination of the splitter plate (cm)
x_0	Virtual origin of the turbulent kinetic energy source (cm)
y	Vertical distance from the centerline of the mixing layer (cm)

TABLE OF CONTENTS

Page

LIST OF FIGURES

FIGURE Page

LIST OF TABLES

1. INTRODUCTION

1.1 Motivation

Hydrodynamic instabilities, in particular, Rayleigh-Taylor (RT) instability, occur in nature as well as industrial processes and range in time and length scales. Examples of RT instabilities include: Type IA supernova explosions (Gull 1975), geophysical formations of salt domes, effluent discharge into estuaries or rivers, combustion, rotating machinery (Cook & Dimotakis 2001) and inertial confinement fusion (Sharp 1984). RT instabilities are induced in initial perturbations when a heavy fluid is oriented above a light fluid in a gravitational field. In an early theory by Youngs (1984), late-time, self-similar behavior of a buoyancy-driven RT mixing layer has been said to have little or no dependence on initial perturbations of the interface. However, recent experimental findings, including the presented study and others, provide evidence that memory of initial conditions remain in the self-similar regime of a RT mixing layer. The motivation for this research is to provide insight to the role of initial conditions on the development of an RT driven turbulent mixing layer, and ultimately to gain a fundamental insight to the role initial conditions play in the inertial confinement fusion (ICF) process. The basic concept of ICF is to utilize inertia of a fuel mass to provide confinement for thermonuclear burn to occur. More specifically, a spherical ICF capsule composed of a core of low-density gas, usually deuterium-tritium, and surrounded by an ablator shell is imploded to achieve a thermonuclear burn (Lindl 1995). There are two different density materials interfacing with one another under a pressure gradient in ICF, so the stage is set for the development of RT instabilities. Because RT driven turbulence is an efficient mixing process, the RT instabilities

---

This thesis follows the style of *Journal of Fluid Mechanics.*

that form between the fuel and surrounding shell in ICF applications causes increased mixing, which in turn decreases the quantity of fuel available for thermonuclear fusion, and ultimately decreasing the energy yield of the ICF capsule (Lindl 1995). Therefore, a fundamental understanding of the role of initial conditions is crucial in the advancement of ICF applications.

Experimental measurements of turbulence statistics in a low Atwood number ($A_t \approx 7.5\text{x}10^{-4}$), miscible, RT driven turbulent mixing layer presented in this work provide a database of statistical measurements to be used in validation efforts of turbulence models, that will in turn be used for ICF design.

1.2 Background

Since the present experiment centers in grid-generated initial conditions for RT turbulence, an overview of background information for buoyancy-driven turbulence as well as grid-generated turbulence is presented in the following sections.

1.2.1 Buoyancy-driven turbulence

The Rayleigh-Taylor instability is induced when a heavy fluid is positioned above a light fluid, wherein the pressure gradient and the density gradient at the interface of the two fluids oppose one another, such that $\nabla p \cdot \nabla \rho < 0$ (Chandrasekhar 1961). The growth of RT instabilities proceed through three stages of evolution; linear instability (exponential growth), non-linear instability (saturation and mode-coupling), and finally to a self-similar RT mixing layer (Youngs 1984). The governing parameter of the buoyancy-driven RT instability is the Atwood number, given in Equation (1.1), where ρ_h and ρ_l are the densities of the heavy and light fluids, respectively.

$$A_t = \frac{(\rho_h - \rho_l)}{(\rho_h + \rho_l)} \tag{1.1}$$

An Atwood number of 1 corresponds to an infinite density difference and an Atwood number of 0 corresponds to no density difference. The structures that form from the perturbations at the interface of the two fluids in the RT driven mixing layer include the bubbles of light fluid rising into the heavy fluid, and spikes of heavy fluid falling into the light fluid. As the bubbles and spikes rise and fall, shearing occurs at the interface of the two structures which cause turbulent mixing to occur (Kraft 2008). At low Atwood numbers, the bubbles and spikes grow at the same rate and form a symmetric mixing layer. But at high Atwood numbers ($A_t \approx 0.1$), the bubbles and spikes grow at different rates, so an asymmetric mixing layer is formed (Banerjee 2006).

During the self-similar growth regime of the small Atwood number RT driven turbulent mixing layer, the penetration height of the bubbles or spikes grow quadratically with time, according to Equation (1.2) (Youngs 1984), where h is the mixing layer half-width, α is the growth parameter, A_t is the Atwood number, g is gravitational acceleration and t is time.

$$h = \alpha A_t g t^2 \tag{1.2}$$

Experimentally measured values of the growth parameter, α, have ranged from 0.044 to 0.07 (Ramaprabhu & Andrews, 2004).

1.2.2 Grid-generated turbulence

A canonical type of turbulence is that of homogeneous isotropic turbulence. Statistically speaking, homogeneous turbulence is defined as statistically invariant under translations in the origin of the coordinate system. Similarly, statistically isotropic turbulence is defined as being statistically invariant under rotations and reflections of the coordinate system (Pope 2000). For the turbulence community, homogeneous isotropic turbulence provides an assumption which simplifies turbulence equations. Experimentally, perfectly homogeneous isotropic turbulence is difficult to obtain, but approximate homogeneous isotropic turbulence can be achieved. Approximate homogeneous isotropic turbulence can be generated by a number of different

configurations and geometries, including; bi-planar grids, perforated plates or stamped plates (Mohamed & LaRue 1990; Roach 1987). Active and passive are two classifications of grid turbulence generators, where an active grid passes through a stationary body of fluid at a constant velocity and passive grid remains stationary while the fluid is passed through the grid at a constant velocity. Turbulence generated by a grid is usually divided into three regions; the anisotropic "setup" region, the nearly isotropic region and the "final period of decay" region (Mohamed & LaRue 1990). The anisotropic "setup" region is caused by the interaction of the jets and wakes created by the grid which produces turbulent kinetic energy. Next, the production of turbulent kinetic energy ceases, so the turbulent kinetic energy begins to decay and the turbulent fluctuations become nearly isotropic and homogeneous. The "final period of decay" takes place when inertial forces become negligible and the viscous forces serve as the primary dissipation mechanism (Mohamed & LaRue 1990).

1.3 Previous experiments

Relevant, previous experiments of RT driven turbulence and grid-generated turbulence are discussed next.

1.3.1 Rayleigh-Taylor

A variety of methods to orient two fluids in an unstably stratified manner have been used in experimental studies of RT driven turbulence. The experiments of Read (1984), Dimonte and Schneider (1996) and Andrews and Spalding (1990) are discussed to give examples of experimental setups to obtain an unstable stratification. The experimental setup of Read (1984) consisted of a tank in which a light fluid was positioned over a heavy fluid to achieve a stable stratification. Rocket motors were attached to the top of the tank to accelerate the tank downwards at up to 75 times the acceleration due to gravity, which resulted in an unstable interface. The experimental setup of Diomonte and Schneider (1996) was similar to Reads'

setup, except the rocket motors were replaced with a linear electric motor (LEM) which could achieve accelerations up to 200 times that of gravity, as well as variable acceleration. The experimental setup of Andrews and Spalding (1990) consisted of a tank with initial stable stratification of the heavy and light fluids, and then the tank was rotated to achieve an unstable stratification of the heavy and light fluids. The quadratic growth, discussed previously, was measured using visualization techniques for each of these experiments, which allowed measurement of the growth parameter, α. Each of the experiments mentioned measured a self-similar growth of the bubbles and spikes which was quadratic with time, with α's that ranged from 0.040 to 0.070.

Due to the statistical nature of turbulence, experimental statistics are needed for validation of turbulence models. Snider and Andrews (1994) developed a water channel facility at Texas A&M University in which the turbulent statistics of a RT driven turbulent mixing layer can readily be measured. Details on RT driven turbulence experiments in the water channel will be discussed in *1.4.1*, below.

1.3.2 Grid-generated turbulence

Grid turbulence has been experimentally investigated by numerous researchers since 1934 (Simmons & Salter 1934). Measurements of grid-generated turbulence have been taken in a variety of experimental setups, including large and small scale wind tunnels, water channels, and even small table top setups. Several different grid types and geometries have been used in both large and small Reynolds number flows. Experiments using bi-planar grids (usually constructed of either square bars or round rods) to generate grid turbulence were most common (Batchelor & Townsend 1948*a*; Comte-Bellot & Corrsin 1966; Ling & Huang 1970; Mohamed & LaRue 1990). Another type of obstruction to generate grid-like turbulence were perforated plates, in which a sheet of material is perforated with an array of holes, typically circular in geometry, in a

regular pattern (Liu, Ting, & Rankin 2003; Roach 1987). A unique method to generate grid-like turbulence was employed by Gad-el-Hak and Corrsin (1974), in which an array of hollow brass pipes made up a jet grid. Each brass pipe had an array of small holes from which a secondary blower forced the formation of jets that could be directed either cross-stream or down-stream (Gad-el-Hak & Corrsin 1974). All of the previously mentioned experiments were performed using stationary grids, but several other experiments have been performed using active (i.e., grids moved through the fluid) grids to generate grid turbulence. Details on examples of grid turbulence generated by active grids can be found in Mydlarski & Warhaft (1996) and White, Karpetis & Sreenivasen (2001). Regardless of the type or geometry of the obstruction used to generate the turbulence, the common goal among all grid turbulence experiments is to generate approximately homogeneous and isotropic turbulence.

Depending on the Reynolds number of the flow, approximately homogeneous and isotropic turbulence is reported to be reached at a distance, x, downstream of the obstruction ranging from $10M$-$50M$ (Ling & Huang 1970; Comte-Bellot & Corrsin 1966), where M is the grid spacing, or the distance between the centerlines of each rod. A diagram can be seen in Figure 1.1 (Taylor 1935). According to Laws and Livesey (1978), grids with a grid solidity ratio, σ (defined in Equation (1.3) (Lavoie *et al.* 2005)), of approximately 0.3-0.4 are typically used to generate turbulence that is homogeneous and isotropic at sufficiently large distances downstream from the grid.

$$\sigma = \frac{d}{M}\left(2 - \frac{d}{M}\right) \tag{1.3}$$

Grids with large solidity ratios, above 0.5, tend to generate less homogeneous, isotropic

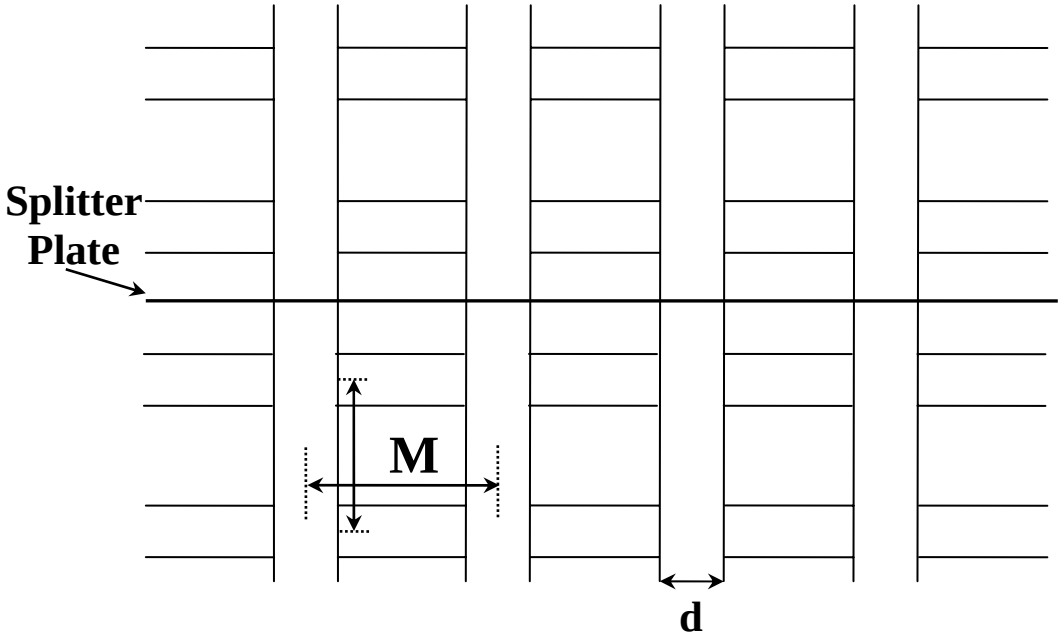

Figure 1.1. Schematic of the bi-planar grid with the definitions of the rod diameter (*d*) and the grid spacing (*M*) illustrated.

turbulence, and it is suggested that the use of grids with high solidity ratios should be avoided (Roach 1987).

The turbulent energy generated by a grid decays due to dissipative nature of the inertial and viscous forces when the production of turbulence has ceased. The turbulent energy decays according to a power-law given by Equation (1.4), where $\overline{K}$ is the time-averaged turbulent kinetic energy, U_m is the mean velocity, A is the decay coefficient based on initial conditions of the flow (Mohamed & LaRue 1990), x is the downstream distance, x_0 is the virtual origin, M is the grid size, and n is the decay exponent (Pope 2000).

$$\frac{\overline{K_{GT}}}{U_m{}^2} = A\left(\frac{x - x_0}{M}\right)^{-n} \tag{1.4}$$

The virtual origin, x_0, is used to account for the fact that the effective origin of the turbulent velocity fluctuations may not coincide with the location of the grid (Mohamed & LaRue 1990) The turbulent kinetic energy term, $\overline{K_{GT}}$ in Equation (1.3) is often replaced with the time-averaged variance of either the stream-wise velocity component, $\overline{u'^2}$, or the vertical velocity component, $\overline{v'^2}$. It has been shown that use of either definition yields similar decay exponents, n. (Lavoie, Burattini, Djenidi, & Antonia 2005). Values of the decay exponent, n, for the turbulent kinetic energy (or the variance of the velocity component) in the approximately homogeneous and isotropic regime have been reported to range from 1.0-2.0 (Batchelor & Townsend 1948*a*; Ling & Huang 1970). Mohamed and LaRue (1990) stated that the decay exponent was independent of initial conditions when the virtual origin, x_0, and the decay exponent, n, were set to values of 0 and 1.30, respectively.

1.4 Texas A&M RT water channel experiments

1.4.1 Rayleigh-Taylor

A water channel facility at Texas A&M University was developed to study low Atwood number buoyancy-driven turbulence. The unstable stratification of the fluids was accomplished by orienting a stream of heavy fluid (cold water) above a light fluid (warm water), and initially separating the two streams with a splitter plate. Upon the termination of the plate, the two streams were allowed to mix and form a statistically steady RT driven turbulent mixing layer, from which turbulence statistics could be measured.

The facility was initially developed and verified by Snider and Andrews (1994). A visualization technique using dye as a fluid marker was developed to obtain a quantitative, statistical measurement of the self-similar growth parameter for the RT driven turbulent mixing layer. The established value of the self-similar growth parameter for the water channel facility is 0.07. Further experiments were performed in the water channel facility by Wilson and Andrews (2002), in which spectral measurements taken for density fluctuations within the RT driven turbulent mixing layer using a high-resolution thermocouple system developed for the facility. Also, Ramaprabhu and Andrews (2004) obtained measurements of velocity statistics within the RT driven mixing layer using a PIV system. Ramaprabhu and Andrews determined that the large growth parameters measured in the water channel facility were due to the presence of long wavelengths in the experiment.

An experimental investigation of the initial conditions of the water channel facility has been performed by Meuschke *et al.* (2006), in which the main focus was to evaluate the velocity and density statistics of the initial perturbation seen in the water channel facility.

The current study utilizes the established diagnostic techniques developed for the Texas A&M RT water channel to evaluate the self-similar growth parameter of the RT driven turbulent

mixing layer, and velocity statistics for the free stream as well as the turbulent mixing layer for the various initial conditions investigated.

1.4.2 Grid turbulence in the Texas A&M RT water channel

Small-scale "grid-type" turbulence has been generated in the water channel facility by previous researchers by installing a very fine grid with a grid solidity ratio of 0.69, perpendicular to the flow direction at the termination of the splitter plate (Ramaprabhu 2003). The motivation for the placement of a fine grid at the termination of the splitter plate was to decrease the momentum deficit at the end of the splitter plate caused by the formation of boundary layers on the splitter plate. This fine grid does not completely eliminate the momentum deficit at the end of the splitter plate, which causes a small wake to form at the interface of the two streams, which is quickly amplified by the buoyancy-driven mixing layer (Ramaprabhu 2003; Mueschke *et al.* 2006). Although the vertical momentum transport due to the buoyancy-driven mixing layer serves to quickly dissipate the small momentum deficit at the termination of the splitter plate, the initial condition of a wake at the interface of the two fluids is inherently present and difficult to parameterize (Mueschke *et al.* 2006).

In the present research, larger scale grid-generated turbulence is generated using coarser grids (rods) to provide a turbulent initial condition of greater magnitude than that of the previously used fine grid. Using a coarser grid to generate a more turbulent initial condition enables the initial conditions to be parameterized with little difficulty. When comparing traditional grid-generated turbulence with the grid-generated turbulence in the current study, a few differences should be pointed out, with the first being the grid. Traditional grid-generated turbulence is typically generated using a bi-planar grid, constructed of rods or bars that are circular or square in cross-section with a solidity ratio between 0.3-0.4, as stated previously. The traditional grid configuration has been shown to generate turbulence with the greatest degree of

homogeneity and isotropy. The current investigation utilizes similar bi-planar grids constructed of rods which have a circular cross-section, which differ from the traditional grid in the grid solidity ratio. The grids implemented for this study have a grid solidity ratio of 0.75, which according to Roach (1987) and Laws & Livesey (1978), could generate flow instabilities as well as turbulence with a lower degree of homogeneity and isotropy than that of the lower solidity ratio grids. The reason for the difference in grid solidity ratios is motivated by one of the objectives for the current research, which will be discussed in *1.5*. Another difference between classical grid-generated turbulence studies and the current investigation is the evaluation region of the power-law decay exponent, n (defined by Equation (1.4) in *1.3.2*). Further details on the grids utilized for the current investigation and the evaluation of the decay exponent will be discussed in *2.1* and *4.3.1*, respectively.

1.5 BHR turbulent transport model

It has long been a goal for the turbulence community to develop engineering models that completely describe and accurately predict the complex dynamics that occur in turbulent flows. Because of the broad range of turbulent flows possible, it is difficult to produce a single model that can quantitatively and accurately describe the turbulent quantities of interest. For this reason, several engineering models have been developed and implemented to model various types of turbulent flows.

The BHR turbulent transport model is a single-point, variable density, model that was developed by Besnard, Harlow, and Rauenzahn (Besnard *et al.* 1987). The BHR transport equations for second order correlations derived from the Reynold's averaged Navier-Stokes equations include the turbulent mass-flux, the density self-correlation and the Reynolds stresses (Steinkamp 1996). The BHR turbulent transport model is applicable for buoyancy driven turbulence applications, and if buoyancy terms are not present the model reduces to the well-

known K-ε model. Closure of the BHR model was obtained by the application of gradient-type diffusion approximations to some, but not all, second order and higher correlations (Steinkamp 1996). Complete transport equations for the BHR turbulent mix model and closure techniques can be found in Besnard *et al.* (1992) and can be supplemented by Steinkamp's Ph.D. dissertation (1996).

The BHR turbulent transport model is implemented in the RAGE (Radiation Adaptive Grid Eulerian) hydrodynamic code, developed at Los Alamos National Laboratory, to transport the turbulent kinetic energy, $\overline{K_{GT}}$, the turbulent length scale, $\overline{S}$, the turbulent mass flux, a, as model variables (Gittings *et al.* 2006) to describe the turbulent diffusion taking place between the different species.

Details on the BHR model equations and their implementation into RAGE is found in Appendix G. The initialization of the BHR turbulent mix model is discussed in *4.4*.

1.6 Objectives

The two objectives presented for the current research include:

1. To generate a turbulent initial condition and quantitatively determine if the late-time development of a low Atwood number buoyancy-driven RT mixing layer can be altered by changing the initial conditions.
2. To experimentally measure turbulence statistics of a low Atwood number buoyancy-driven RT mixing layer to provide an experimental data set to be used in the performance evaluation of the variable-density, RANS type, BHR turbulent transport model.

An existing water channel facility at Texas A&M University has been used to carry out the research objectives. The water channel facility achieved the necessary unstable stratification by

orienting cold (heavy) water above warm (light) water. The following tasks were required to accomplish the objectives, including:

a) Determine a method to change initial conditions in the water channel facility.

b) Demonstrate a change in late-time development of a low Atwood number buoyancy-driven RT mixing layer.

c) Obtain initial values of turbulent kinetic energy, turbulent length scale and the power-law decay exponent for initialization of the BHR turbulent transport model.

d) Evaluate the performance of the BHR turbulent transport model by comparing model and experimental results.

Next, a description of the experimental setup and measurement diagnostics are given.

2. EXPERIMENTAL SETUP AND MEASURMENT DIAGNOSTICS

2.1 Description of experimental facilities

The current experimental investigation was conducted in an existing water channel facility at Texas A&M University. Testing and design of the water channel is described in detail in Snider and Andrews (1994), and more recently in Ramaprabhu and Andrews (2004). A brief description of the flow channel, its operation, and the relevant equipment are given.

The flow channel is an open loop system which consists of an entrance plenum, a test section, and an exit plenum. A schematic of the experimental flow channel is shown in Figure 2.1. Two parallel streams of hot (upper) and cold (lower) water enter the channel from two supply tanks, each with an 1890 liter (500 gallon) capacity. A temperature difference for the two streams of approximately 5 $^{\circ}C$ is used in this investigation. To obtain the Atwood number of the experiments, temperature measurements were converted to density using an equation of state defined by Equation (2.1) (Kukulka 1981).

$$\rho(T) = \frac{\begin{pmatrix} 999.8396 + 18.2249T - 0.007922T^2 - 55.448\times10^{-6}T^3 \\ +149.756\times10^{-9}T^4 - 393.295\times10^{-12}T^5 \end{pmatrix}}{1+18.159\times10^{-3}T} \tag{2.1}$$

The flow rates of the two streams are regulated using control valves and calibrated rotameters. Sump pumps are used in each of the supply tanks to ensure the water in the tanks does not undergo thermal stratification. A Plexiglass splitter plate with a thickness of 0.32 *cm* and a 2.5° knife edge on the downstream end initially separates the two streams in the entrance plenum. To minimize the amount of free stream turbulence a combination of flow straighteners and wire meshes are placed in each stream at approximately 20 *cm* intervals prior to the termination of the splitter plate (Snider and Andrews 1994). For a fine grid experiment, an extra mesh was placed

at the end of the splitter plate, which serves to reduce the momentum deficit caused by boundary layers on the splitter plate, which were found to be approximately 3-4 *mm* thick (Mueschke 2004). Upon the termination of the splitter plate, the two streams mix in the test section. To induce unstable stratification (RT instability), the two streams enter the test section with the cold (heavy) fluid on top and the hot (light) fluid on bottom. The dimensions of the test section are 100 *cm* in length, 20 *cm* deep, and 32 *cm* in height. Operating procedures for the water channel are given in Appendix A.

A stationary, bi-planar grid with a high solidity ratio, σ, constructed of acrylic rods (cylindrical in cross-section) is positioned perpendicular to the flow at the termination of the splitter plate. Three different grids are used for the current investigation, which are seen in Figure 2.2 with the fine, medium, and coarse grid from left to right. Experimental parameters and grid properties for the three different initial conditions are given in Table 2.1. The bi-planar grids can be positioned in two different orientations for the current study and can be seen in Figure 2.1, where the splitter plate divides the two middle rods in orientation one the splitter plate divides center rod in orientation two. All results presented in the current research were measured with the grids in orientation 1, unless otherwise stated.

Measurements of velocity and density statistics are necessary to meet the objectives for the current investigation, and so several measurement techniques are employed. The height of the mixing layer, which is required to evaluate the growth parameter, α, is measured from using a visualization technique outlined in Snider and Andrews (1994) as well as Banerjee (2006). Velocity statistics, used to parameterize the initial conditions of the experiments, are measured using particle image velocimetry (PIV).

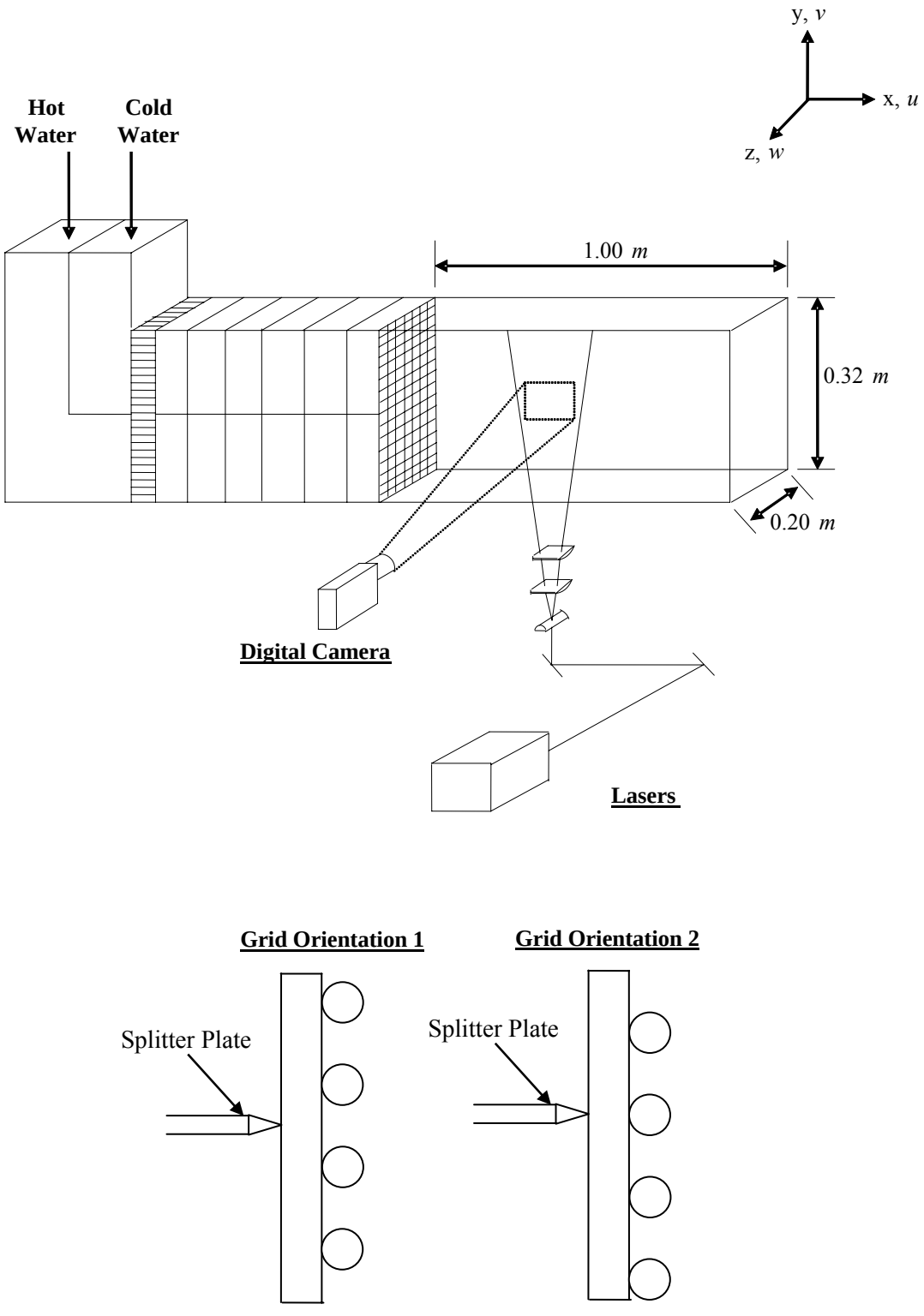

Figure 2.1. Schematic of the experimental apparatus and the different grid orientations considered along with the coordinate system for the investigation and the setup of the diagnostics.

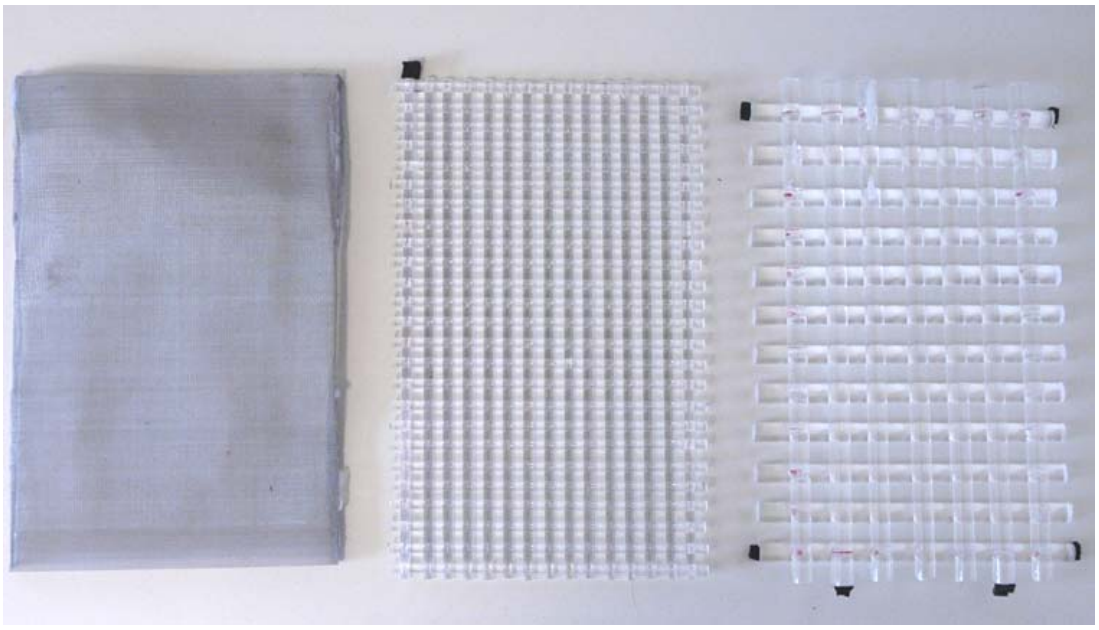

Figure 2.2. Digital photograph of the three different grids used for this experiment. From left to right is the fine grid (d=0.028 *cm*), the medium grid (d=0.635 *cm*) and the coarse grid (d=1.270 *cm*).

	Nomenclature (Units)	**Fine Grid**	**Medium Grid**	**Coarse Grid**
Rod Diameter	d (*cm*)	0.028	0.635	1.27
Grid Spacing	M (*cm*)	0.064	1.27	2.54
Grid Solidity Ratio	σ	0.69	0.75	0.75
Mean Velocity	U_m (*cm/s*)	4.50 – 5.50	4.50 – 5.50	4.50 – 5.50
Atwood Number	A_t ($x10^4$)	7.0-7.5	7.0-7.5	7.0-7.5
Grid Reynolds Number	Re_M	28-35	600-700	1200-1400
Kinematic Viscosity	ν (cm^2/s)	0.01	0.01	0.01

Table 2.1. Summary of experimental parameters for the fine, medium and coarse grid setups.

2.2 Measurement diagnostics

2.2.1 Visualization technique

Quantitative measurements and qualitative observations are made in the water channel using the visualization technique originally developed by Snider and Andrews. As with Snider, the top stream (heavy fluid) is marked with a Nigrosene dye. The channel is backlit using six fluorescent lights. To diffuse the light and to provide a more uniform background, a prismatic sheet and a sheet of matte acetate paper are placed between the light bank and the back wall of the channel. Monochrome photographs of the experiment are taken using a Cannon A80, 4 megapixel digital camera with a resolution of 1024 x 768. Aperture, shutter speed, and ISO settings are set manually before each experiment to 7.1, 1/60, and 100, respectively. The digital camera is also set on "continuous burst" mode to allow the experiment to be photographed at a constant rate of 60 photographs per minute.

For the current study, Beer Lambert's Law, defined by Equation (2.2), is used to relate the volumetric concentration of dye to the absorption of monochromatic light from its source, I_o, across path length z, where κ is the monochromatic extinction coefficient and ω is the absolute extinction coefficient for the medium. Expanding the exponential in a series and retaining the first term for small values of the exponential extinction coefficient gives a linear relation between intensity and extinction coefficient (Banerjee 2006).

$$I_m = I_0 \exp\left(-\int_0^z \kappa dz\right) \approx I_0 \left[1 - \int_0^z \kappa dz\right] = I_0 (1-\omega) \tag{2.2}$$

To relate pixel intensity to the concentration of dye, the wedge calibration technique described in Snider and Andrews (1994) is used. A detailed description of this calibration procedure is found in Appendix B. To ensure a linear absorption behavior, the concentration of the dye must be measured prior to each experiment. The chlorine levels in the supply water for the experiments vary drastically, which in-turn alters the absorption behavior of the dye. To alleviate this

problem, 50 mL of Sodium Thiosulfate is added to each tank prior to adding the dye to lower the chlorine content of the water.

Non-uniform backlighting of the channel is corrected by taking an ensemble average of approximately ten images of the water channel with no dye present and then subtracting it from the ensemble average of approximately 150 mixing layer images. A global shift of the image intensities during the averaging process is also performed to eliminate the effect of the fluctuating intensities caused by the fluorescent light banks. This global shift is performed by averaging the light intensity of a small representative square of pixels (≈ 10x10 pixels) close to the splitter plate (≈ 5 cm downstream of the splitter plate) in the lower, unmarked portion of the channel for the background image and comparing it to the averaged light intensity for the same location for each of the instantaneous mixing layer digital images. Care is taken to ensure the absence of any marked fluid in the instantaneous mixing layer image by keeping the global shift square near the bottom of the water channel. If a difference in the background intensity and the mixing layer image intensity exists, then a global intensity shift (either increased or decreased) is performed on the entire mixing layer image to equalize the intensities of the background image and the instantaneous mixing layer image. Histograms of the uncorrected average mixing layer image and the corrected averaged mixing layer image are seen in Figure 2.3 (a-b). Comparing the uncorrected (a) with the corrected (b) histogram, the corrected (b) histogram shows sharp peaks that indicate the outside of the mixing layer while the uncorrected (a) histogram shows a sharp peak on the dark side, but a broad peak on the bright side due to the non-uniform backlighting of the channel. The corrected ensemble averaged mixing layer image provides a matrix of intensities which will be used to determine a time evolution of the mixing layer heights, mixture fraction profiles at various stages in the evolution of the mixing layer, and the growth parameter, α, of the self-similar region of the mixing layer for each initial condition.

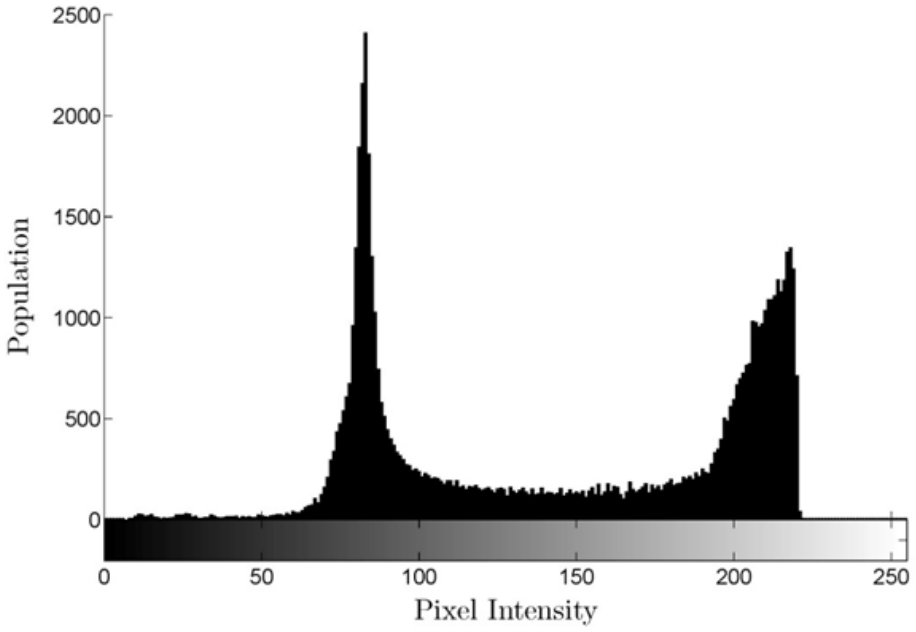

(a)

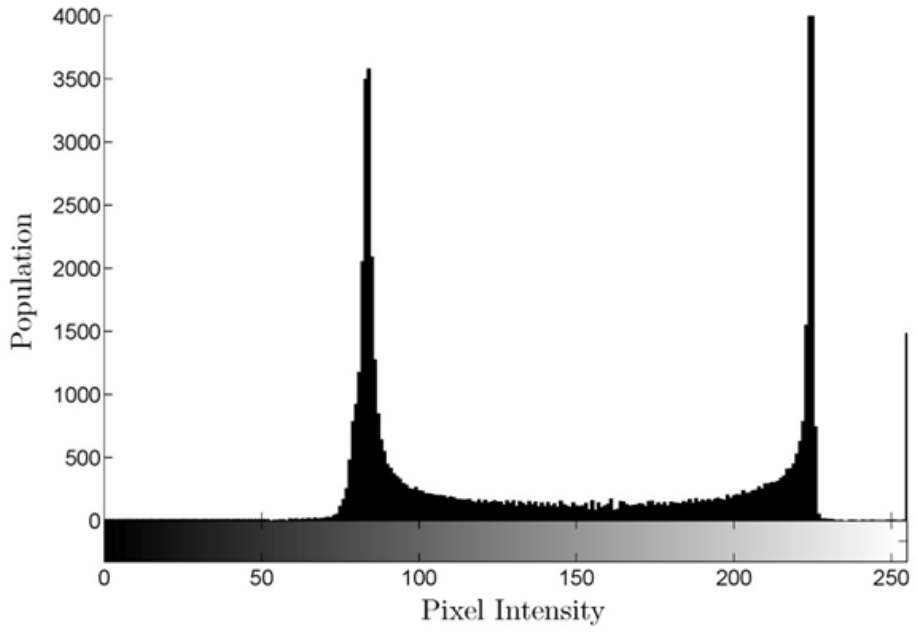

(b)

Figure 2.3. Histograms of the pixel intensities for the ensemble averaged mixing layer image for the fine grid experiment before (a) and after (b) the background correction is applied.

2.2.2 Particle image velocimetry

PIV is used to measure velocity statistics both inside and outside the mixing layer. The PIV system is made up of two 120 *mJ* Nd-Yag lasers, each with a firing frequency of 15 *Hz*. The pulses of the two lasers are alternated to obtain an effective sampling frequency of 30 Hz for the entire PIV system. Each stream is seeded with approximately 5-7.5 *mL* per 500 *gallons* of Conduct-O-Fil silvered, hollow glass spheres (Potters Industries Inc.) that are approximately 10 μm in diameter. The laser beam is directed through a series of cylindrical lenses that serve to spread the laser into a sheet, approximately 1 *mm* in thickness at the interrogation window, and orient the sheet vertically through the channel. The seed particles are captured with a KODAK Megaplus digital camera.

The laser pulses and the camera are triggered synchronously using a pulse generator. The pulse generator takes the 30 *Hz* triggering frequency from the digital camera and divides it into two 15 *Hz* frequencies that are precisely 180˚ out of phase with one another, and sends one signal to each of the lasers to trigger the flash lamp. Operating procedures for the pulse generator are found in Appendix E, and further details of the setup of the triggering system are found in Kraft (2004). A LabVIEW data acquisition system is used to record 1200 images at a resolution of 640x480 pixels. Post processing of the data is performed with MatLAB software using the MatPIV program, which exploits a cross-correlation function to determine a velocity field from any two consecutive images (Grue *et al*. 2000). The cross-correlation function, $R(x, y)$, defined in Equation (2.3), is used to determine the particle displacement between two consecutive images, Im_1 and Im_2.

$$R(x, y) = \sum_{i=M/2,\, j=N/2}^{M/2} \mathrm{Im}_1(i, j)\,\mathrm{Im}_2(i + x, j + y) \tag{2.3}$$

A displacement vector is defined as the distance between the correlation peak and the center of the interrogation window. Any displacement vectors with magnitudes greater than two standard deviations of the neighboring vectors are substituted with an interpolated vector. The MatPIV algorithm includes multiple passes of the cross-correlation routine, in which the first pass is used as an initial guess for the second pass and so forth. Also, there is a 50% overlap with the neighboring image, so the final vector field contains 39x29 vectors. From the 1200 images captured, 1199 vector fields are generated using the method described, which are used to obtain velocity statistics to evaluate initial conditions for each of the grid configurations. A method to determine uncertainty in the PIV velocity measurement is described by Adrian (1997) and was determined to be 0.05 cm/s (Ramapabrahu 2003). Operating procedures for the PIV experiments are found in Appendix D.

3. INITIAL CONDITION EFFECTS ON LATE-TIME RT DEVELOPMENT

Initial conditions were historically thought to have little influence on the development of a buoyancy-driven RT mixing layer, but evidence from the current research provides confirmation that initial conditions do play a role in the mixing layer development. To illustrate the difference between the initial conditions covered for this investigation, a qualitative comparison of the different initial conditions was performed. Also, the utilization of the visualization technique described in *2.2.1* provided a quantitative evaluation of the mixture fraction ($\overline{f}_v$), the mix half-width (h) and growth parameter (α) for each of the initial conditions.

3.1 Qualitative overview of initial conditions

A well known technique for flow-visualization is utilized by introducing a small volume (1 *gallon*) of milk into the 500 *gallons* of warm water. Then, as the fluid flows over the end of the splitter plate, the "surface" of the bottom stream is marked by the milk producing the photographs seen in Figure 3.1 (a-c). Some care needs to be taken with the milk visualization technique since the Schmidt number of milk in water is approximately 700, and the Prandlt number of water is approximately 7, thus the milk is not an accurate marker of density. Figure 3.1 (a-c) shows the RT development from the three grids, with the grid on the left hand side, the flow from left to right, and approximately the first 10 *cm* visible. Upon inspection of the digital images in Figure 3.1 (a-c), several qualitative observations can be made. First, small wave striations seen coming off the splitter plate with the fine grid are caused by a small wake which forms from the momentum deficit caused by the growth of boundary layers on the splitter plate. The wake is quickly amplified by the unstable stratification and undergoes mode coupling and mixing. Also, the structures seen in the mixing layer after the fine grid are more two-dimensional, while the structures seen after the medium and coarse grids are clearly three-

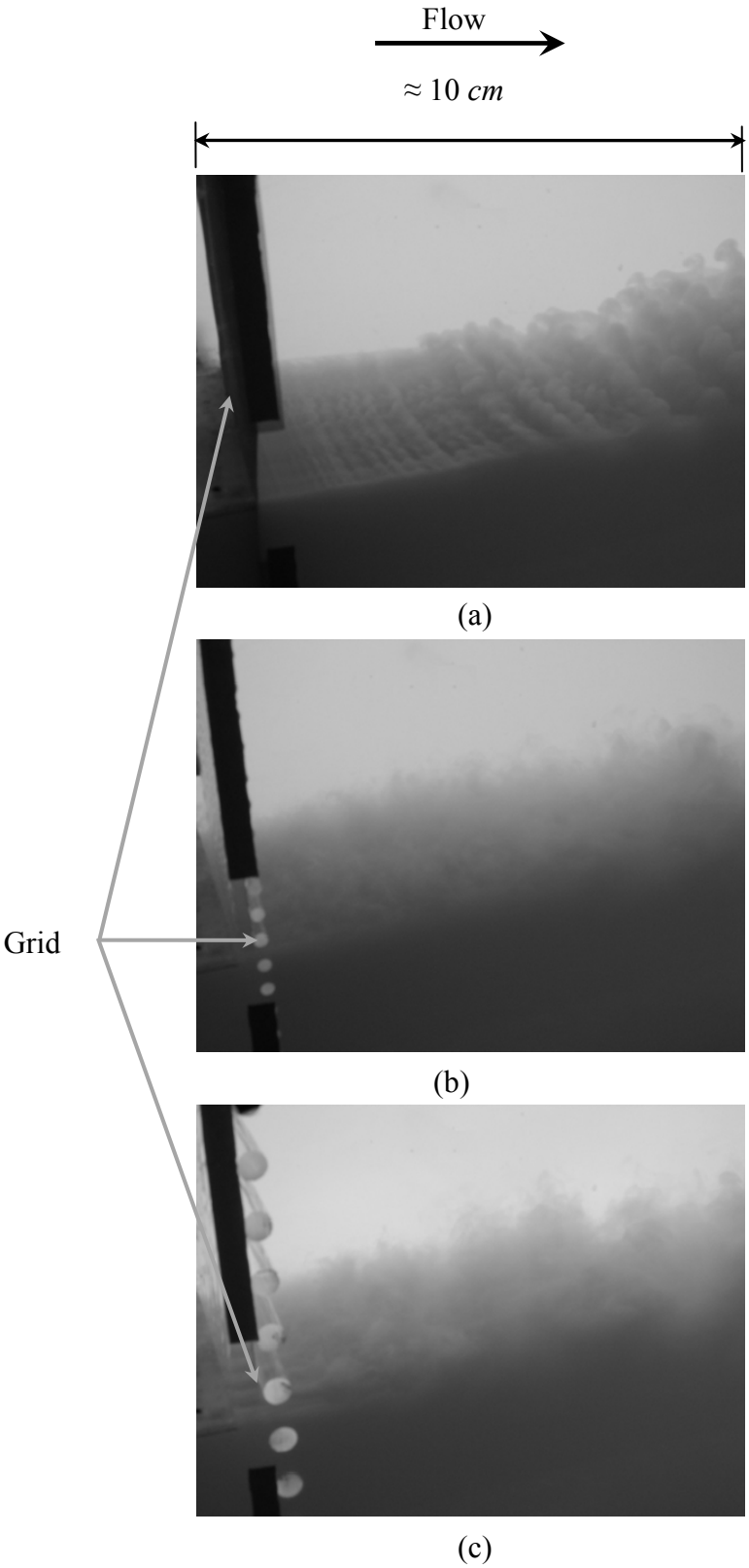

Figure 3.1. Buoyancy-driven mixing layer from the water channel facility with $A_t = 7.2x10^{-4}$ (U_m=4.6 *cm/s*). Bottom (light) fluid is marked with milk, with the viewpoint from a slight downward angle. Flow is from left to right, with the fine mesh (a), the medium mesh (b), and the coarse mesh (c) positioned immediately downstream of the splitter plate.

dimensional. Three-dimensionality of the structures behind the medium and coarse grids is caused by the interaction of the wakes shedding from the larger diameter rods that make up the grids. It can also be seen that the interface of the top and bottom stream immediately after the fine grid is sharp, while the interface of the two streams immediately after the medium and coarse grid is diffuse. The diffuse mixing layer in the medium and coarse grid images is caused by the increased mixing taking place due to the interaction of the wake shedding from the grids and associated broad-band initial perturbation spectrum that the larger grids produce.

3.2 Experimental results and analysis using visualization technique

Figure 3.2 (a-c) show an instantaneous photograph of the buoyancy-driven mixing layer from each of the three experiments with the fine, medium, and coarse grid, respectively. The flow is from left to right with the cold, dyed stream positioned above the warm stream. The top and bottom streams are set to the same velocity, so there is no mixing caused by shear between the two streams. The velocity of the dye experiments ranged from 4.40 *cm/s* to 4.55 *cm/s* with an Atwood number ranging from 7.0×10^{-4} to 7.5×10^{-4}. For each of the three instantaneous images in Figure 3.2 (a-c), a difference can be observed in the initial development of the mixing layers between the medium and fine grid and also between the coarse and the fine grid. Similar to the milk images from Figure 3.1 (a-c), the interface between the heavy (dyed) and light fluid for the fine grid (a) is sharp, whereas the interface for the medium (b) and coarse (c) grids is diffuse, which is caused by the increased amount of mixing from the broad-band grid-generated turbulence.

3.2.1 Mixture fraction measurement

After performing the background correction on the average mixing layer image discussed previously in *2.2.1*, the maximum and minimum pixel intensities (I_{max} and I_{min}) are defined

(a)

(b)

(c)

Figure 3.2. Instantaneous digital images of the mixing layer the fine (a), medium (b), and coarse (c) grids immediately following the termination of the splitter plate. The flow is from left to right with the top and bottom stream velocities matched to approximately 4.5 *cm/s* and Atwood numbers of approximately 7.35×10^{-4}.

from the two peaks on the histogram of the corrected ensemble averaged mixing layer image, as seen in Figure 2.3 (b) in section *2.2.1*. Since the relationship between the concentration and pixel intensity is linear, the average mixture fraction, $\overline{f}_V$, of the mix is defined by Equation (3.1) (Snider & Andrews 1994).

$$\overline{f}_V(x,y) = \frac{I_{corr}(x,y) - \overline{I_{\min}}}{\overline{I_{\max}} - \overline{I_{\min}}} \tag{3.1}$$

The mixture fraction provides a measure of the average volume of each fluid at any point in the mixing layer. The definition sets pure fluids to 1 and 0 for the hot and cold water, respectively. The mixture fraction provides a quantitative measure of the mixing layer width at any point downstream.

3.2.2 Mix width measurement

Using Equation (3.1), the 5%, 50% and 95% mixture fraction contours are superimposed over the corrected ensemble averaged mixing layer image in Figure 3.3 (a-c). Defining the outer edges of the mixing layer as 5% and 95% of the mixture fraction provides a quantitative measure of the width (*w*) of the mixing layer (Banerjee 2006). For low Atwood number RT experiments, the growth of the mixing layer is symmetric about the centerline and therefore, the penetration height (*h*) of the spike or bubble is simply half of the mix width. It can be seen in Figure 3.3 (a-c) that the centerline of the mixing layer (50% contour level) for each of the experiments is horizontal along the length of the test section, which provides a simple indicator of proper inflow/outflow settings for each experiment. Several additional qualitative observations can be made from the mixture fraction contours. In the first half of the test section, the contours of Figure 3.3 (a-c) show a distinct change in the mixing layer development between the fine (a), the medium (b) and the coarse (c) grids. The width of the mixing layer in the first half of the test section for the fine grid is significantly smaller than that of the medium and coarse grids, which

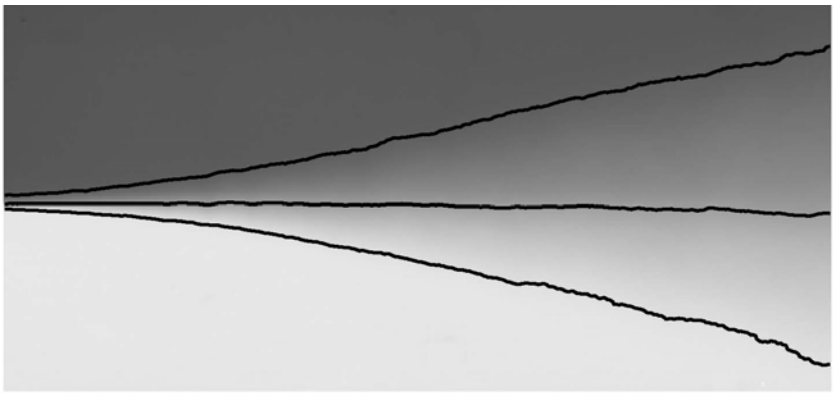

(a)

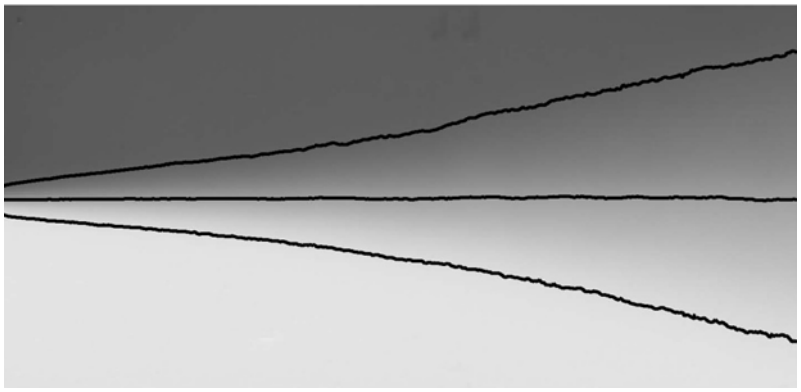

(b)

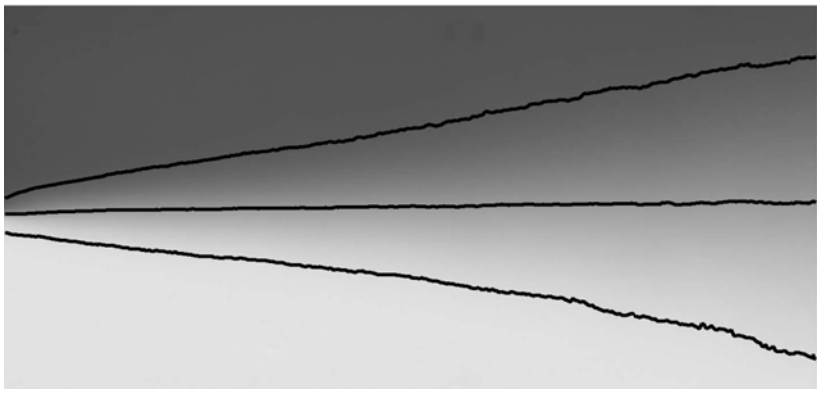

(c)

Figure 3.3. 5%, 50% and 95% mixture fraction contours superimposed over the corrected average mixing layer image from the fine (a), medium (b) and coarse (c) grid experiments. The flow is from left to right with the top and bottom streams matched to a velocity of approximately 4.6 *cm/s* and an approximate Atwood number of 7.3×10^{-4}.

can be attributed to the increased mixing that occurs following the medium and coarse grids due to the grid-generated turbulence. The grid-generated turbulence serves as an initial mixing mechanism which causes the mixing layer to be more diffuse immediately after the grids. Downstream distance is translated to a dimensionless unit of time, τ, which is defined in Equation (3.2), where time is related to distance downstream using Taylor's hypothesis, $t = x/U_m$, and H is the height of the water channel.

$$\tau = \frac{x}{U_m}\sqrt{\frac{A_t g}{H}} \tag{3.2}$$

Evolution of the mixing layer half-width, $(h_b - h_s)/2$, for the fine, medium and coarse grids are shown in Figure 3.4. Since the origin of the mixing layer is at the end of the splitter plate, the grids interfered with the measurement of the mixing half-width at very early times, which resulted in a gap from the end of the splitter plate (τ = 0) to the location where the mixing layer half-width can be measured. Distinct developmental differences between the mixing layer half-width are evident when comparing the medium or coarse grid to the fine grid. Similar to the behavior seen in the mixture fraction contours in Figure 3.3 (a-c), the mixing layer half-width is initially larger for the medium and coarse grids than the fine grid. Also, it should be noted that the mixing layer half-width for the fine grid grows at a faster rate from τ = 1.0 to τ = 1.8 when compared with the growth of the mixing layer half-width for the medium and coarse grids.

Profiles of the mixture fraction at any downstream location for the fine, medium and coarse grids are taken from the ensemble averaged mixture fraction Figure 3.5 (a-c) shows mixture fraction profiles at three separate locations downstream; the initial region (τ = 0.15-0.25), the transition region (τ = 0.85), and the self-similar region (τ = 1.75). As expected, the mixture fraction profiles are mostly linear for each of the grid cases. There are two differences that can be seen between the fine grid experiment, and the medium and coarse grid experiments. The

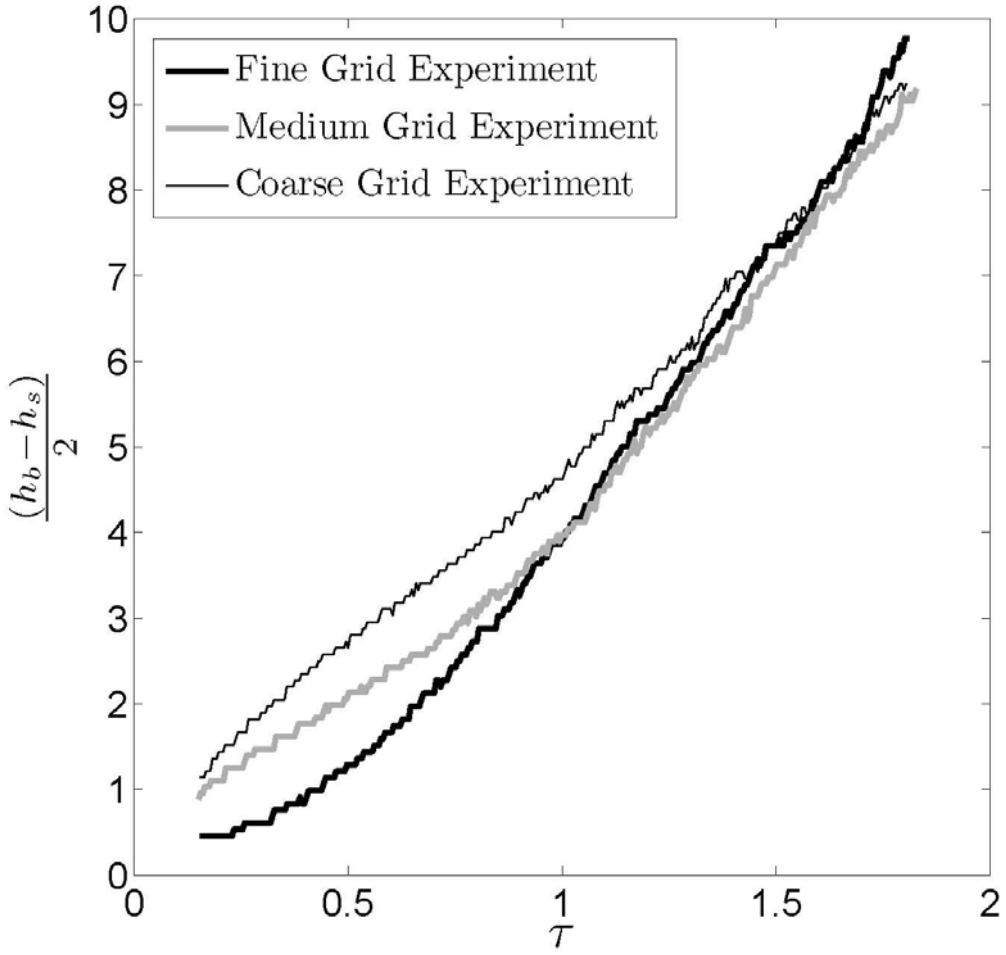

Figure 3.4. Evolution of the mixing layer half-widths evaluated from the visualization technique experiments with the fine, medium and coarse grids placed immediately following the termination of the splitter plate.

first difference is the variation in the sharpness of the interface for the initial mixture fraction profile. The fine grid has a sharper interface than the medium and coarse grids, which can be attributed to the larger amount of turbulent kinetic energy being generated by the medium and coarse grids. A larger amount of turbulent kinetic energy serves as an initial mixing mechanism at the interface of the two streams of the mixing layer. The earliest mixture fraction profile for the coarse grid was evaluated at τ=0.25 rather than τ=0.15 because of interference between the physical grid and the measurement. The second difference between the fine grid experiment and the medium and coarse grid experiments can be seen by looking at the change in height between the transition profile and the self-similar profile. The change in height between the profile at τ = 0.85 and τ = 1.75 is greater in the fine grid experiment than in the medium and coarse grid experiments. Using the mixture fraction measurement for the fine, medium and coarse grid initial conditions, the self-similar growth parameter, α, for each initial condition can be evaluated.

3.2.3 Growth parameter (α) measurement

As the mixing layer develops, it forms a self-similar mixing layer which grows quadratic with time (i.e. distance downstream in the present experiment) according to Equation (1.2), where h is the half-width of the mixing layer, α is the growth parameter of the mixing layer and A_t is the non-dimensional density difference between the two streams. Using the measured height of the mixing layer, the growth parameter, α, was evaluated to determine if a change in the behavior of the mixing layer occurred when the initial conditions were altered. The method employed to measure the growth parameter was to plot the non-dimensional height, h/H, of the mixing layer versus the non-dimensional downstream distance, $A_t g t^2/H$, where the slope provides an evaluation of $d(h)/d(A_t g t^2)$ in the self-similar region of the turbulent mixing layer. The height, H, of the water channel was used to non-dimensionalize the mixing height and downstream

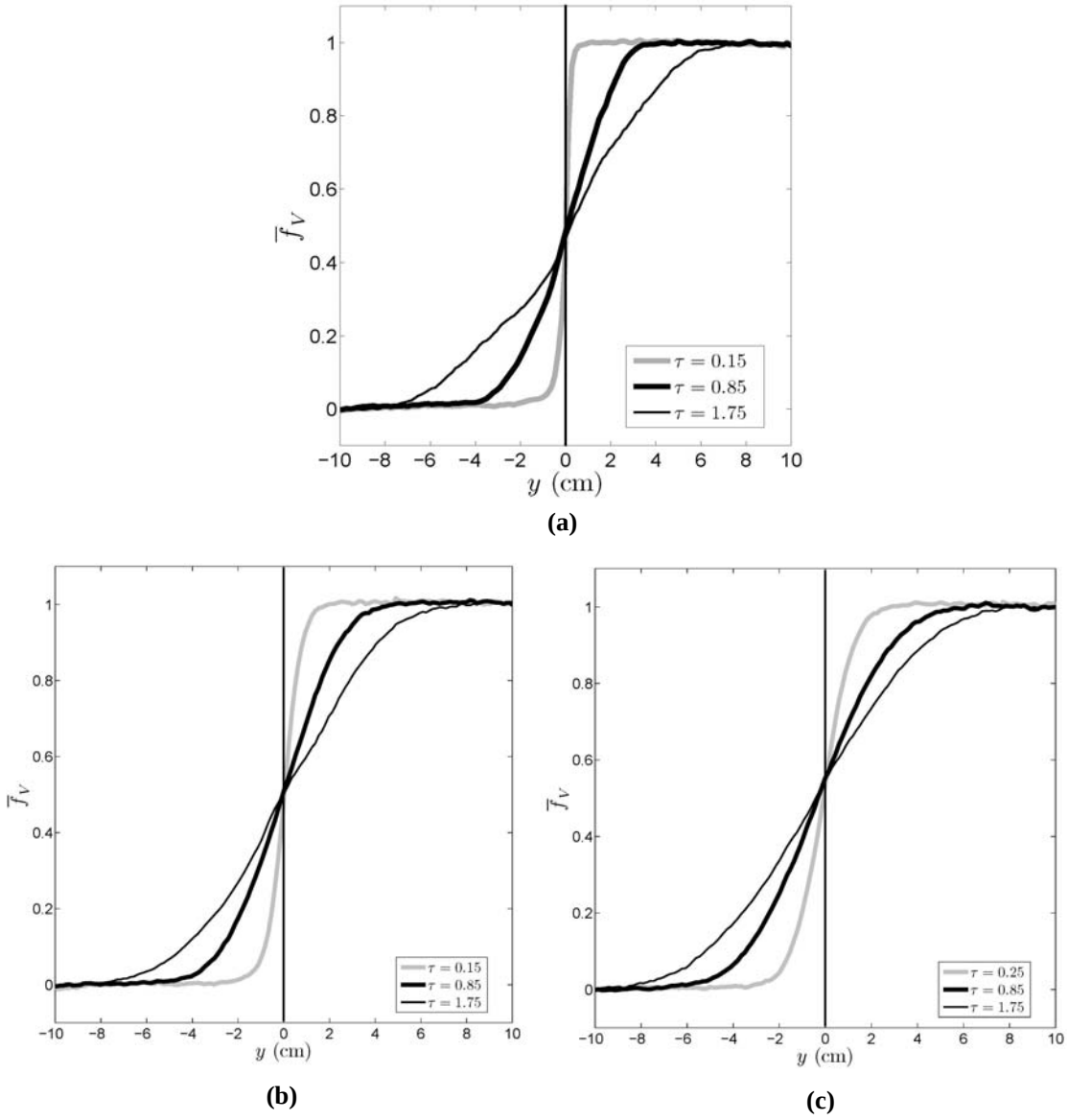

Figure 3.5. Profiles of the mixture fraction vertically across the mixing layer at non-dimensional downstream locations of τ=0.15-0.25, τ=0.85 and τ=1.75 for the fine (a), medium (b), and coarse (c) grid experiments.

distance. The self-similar region of the flow is defined from $\tau \approx 1.4\text{-}1.8$, which corresponds to $A_t g t^2/H \approx 2.0\text{-}3.3$. To ensure the facility was working properly, a validation experiment to measure the growth parameter, α, with the fine grid at the end of the splitter plate was performed. The established value of α for the fine grid at the end of the splitter plate in the Texas A&M water channel facility is 0.07. The growth constant measured in the verification experiment with the fine grid at the end of the splitter plate is 0.072 ± 0.003, which verifies the operation of the water channel. An example of the linear fit used to determine the growth parameter measurement for the fine grid initial condition is seen in Figure 3.6.

Experiments were performed to measure the growth constant in the medium and coarse grid cases. The measured growth parameter for the medium and coarse gird experiments can be seen in Figure 3.7. A change in the values of the growth parameter for the mixing layer height, α, is observed between the fine grid experiment and the medium and coarse grid experiment. The newly measured growth parameters for the medium and coarse grid are 0.063 ± 0.003 and 0.060 ± 0.03, respectively. The change in growth parameters for the medium and coarse grid suggests that manipulating the initial conditions of the RT mixing layer provides a means to alter the behavior of the mixing layer. Historically, for the late time self-similar regime of this type of flow, the memory of initial conditions was said to be lost and have no effect on the growth parameter.

A set of experiments to determine if grid orientation for the medium and coarse grid had an effect on the self-similar growth parameter (α) was performed with the grids in orientation 2, as illustrated in Figure 2.1 of section *2.1*. The growth parameter did decrease from the value measured with the medium and coarse grids in orientation 1, but they did so within the experimental uncertainty. Details of the analysis for the set of experiments with the medium and coarse grids in orientation 2 can be found in Appendix C.

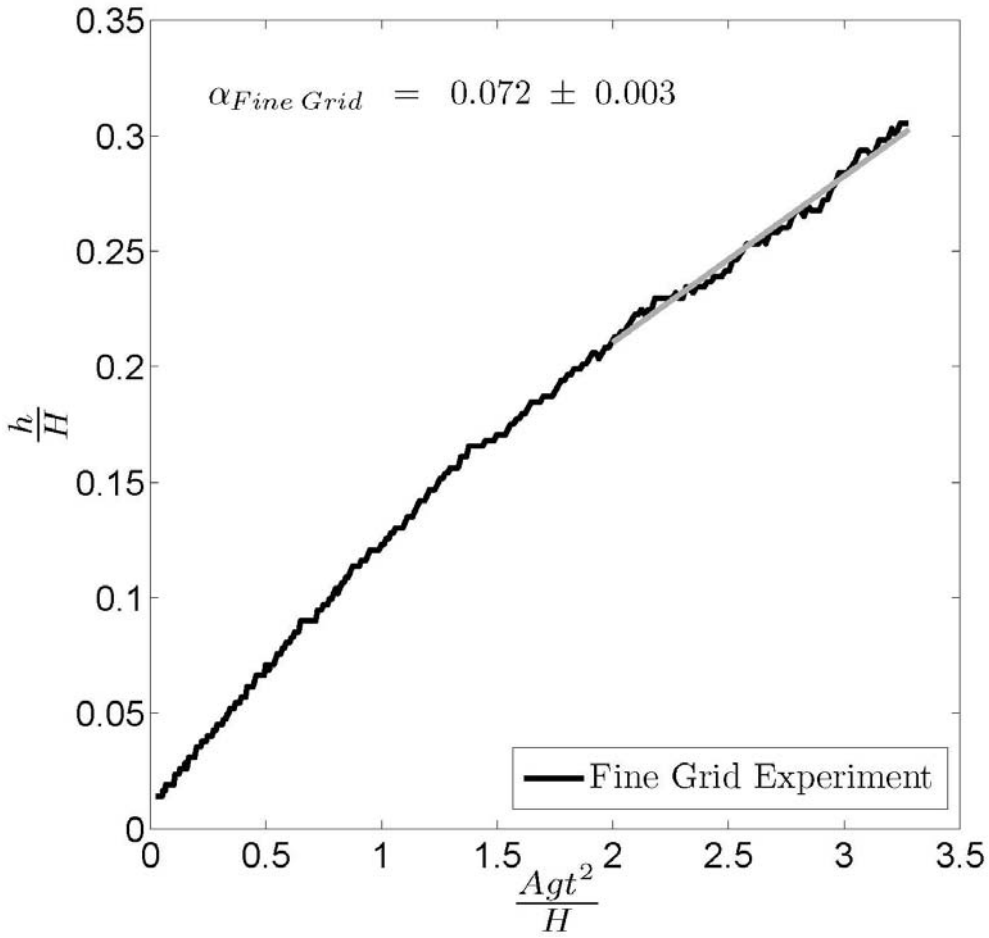

Figure 3.6. Mixing layer half-width as a function of A_tgt^2 for the experiment with the fine grid placed immediately following the termination of the splitter plate. Plot is non-dimensionalized by channel height, *H*.

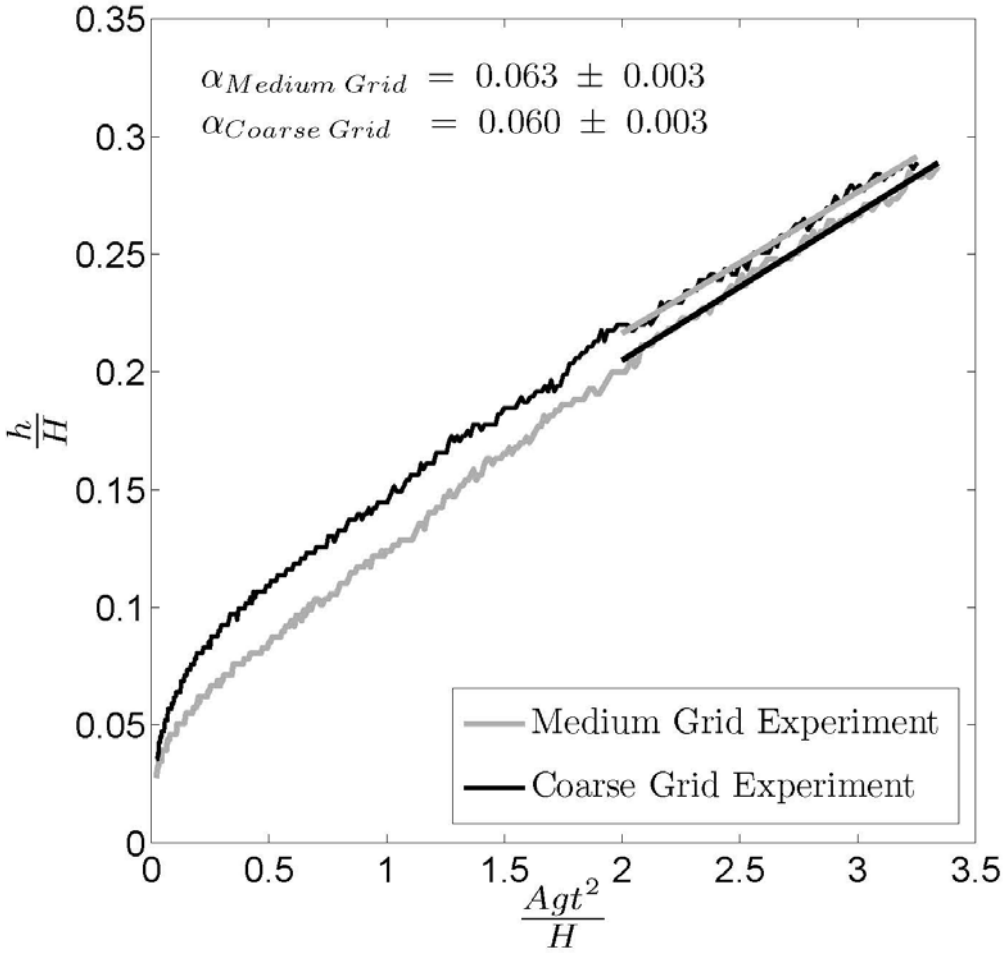

Figure 3.7. Mixing layer half-width as a function of A_tgt^2 for the two separate experiments, one with the medium grid and another with the coarse grid placed immediately following the termination of the splitter plate. Plot is non-dimensionalized by channel height, *H*.

4. VALIDATION WITH GRID TURBULENCE

4.1 Verification of grid-generated turbulence

As discussed in *1.4*.2, the high solidity ratios of the medium and coarse grids generate less isotropic turbulence. So, verification experiments were performed to ensure the generation of acceptable magnitudes of isotropic turbulence from the grids. Before a stationary grid can produce approximately isotropic turbulence, there is an initial setup period through which the turbulence must pass before it can be considered isotropic. Also, isotropic turbulence is homogeneous in nature, so if the flow is shown to be isotropic, then it will be assumed homogeneous. The isotropy of grid-generated turbulence can be measured in several different ways. Mohamed & LaRue (1990) determined the isotropy of the grid-generated turbulence by determining when the skewness of the velocity approached zero. Another method to measure the isotropy of the flow, and the method employed for the current investigation, is to measure two velocity components and evaluate the ratio of the root mean square (rms) of the axial (*u'*) velocity fluctuations to the vertical (*v'*) velocity fluctuations, $\sqrt{\overline{u'^2}}\Big/\sqrt{\overline{v'^2}}$. The ratio of the velocity fluctuations should be unity if the flow is perfectly isotropic. According to the literature on isotropic grid turbulence, a flow is considered isotropic when $0.95 \le \sqrt{\overline{u'^2}}\Big/\sqrt{\overline{v'^2}} \le 1.05$ (Ling & Huang 1970). In the present experiment, velocity statistics needed to determine whether the flow is isotropic or anisotropic were measured using PIV. The turbulence generated by the medium and coarse grids must go through a "setup" phase, where the flow is anisotropic immediately following the grids. This anisotropy is caused by the interaction of the jets and wakes generated by the grids. The evolution of the ratio of the rms velocity components is shown in Figure 4.1 for the medium grid case, in which the initial setup region for the grid

turbulence generated is indicated as well as where the approximately isotropic region starts. Figure 4.1 shows that for the medium grid experiment, the flow is defined to be approximately isotropic (according to the acceptable range quoted by Ling and Huang) at approximately six grid lengths (x/M) downstream from the splitter plate. Similarly, in Figure 4.2 for the coarse grid experiment, the flow is defined to be approximately isotropic four grid lengths downstream from the splitter plate. Initial PIV measurements immediately downstream of the grids are high resolution (30 Hz) measurements, while subsequent experiments are low resolution (15 Hz) measurements. Verification of the lower resolution PIV measurements is discussed in Appendix F. A grid Reynolds number is defined in Equation (4.1), where U_m is the mean velocity, M is the grid spacing and υ is the kinematic viscosity.

$$\mathrm{Re}_M = \frac{U_m M}{\upsilon} \tag{4.1}$$

The grid Reynolds numbers for the medium and coarse grids are 600-700 and 1200-1400, respectively. Typical grid Reynolds numbers for grid turbulence studies are significantly higher, ranging from 5150-68000 (Mohamed & LaRue 1990). As stated in *1.3.2*, a typical distance required for the grid-generated turbulence to pass through the "setup" phase to the approximately isotropic regime ranges from 10-50 grid lengths downstream from the grid. The grid-generated turbulence measured for the current investigation reached approximate isotropy quickly which can be attributed to the low grid Reynolds number for the flow. The measure of isotropy presented for the medium and coarse grids provides a verification of the generation of approximately isotropic grid-generated turbulence.

4.2 Measurement of initial conditions

By illustrating that initial conditions do have an effect on the development of a buoyancy-driven RT mixing layer, a unique opportunity arises to evaluate the performance of the BHR turbulent transport model. To evaluate the performance of the BHR turbulent transport model,

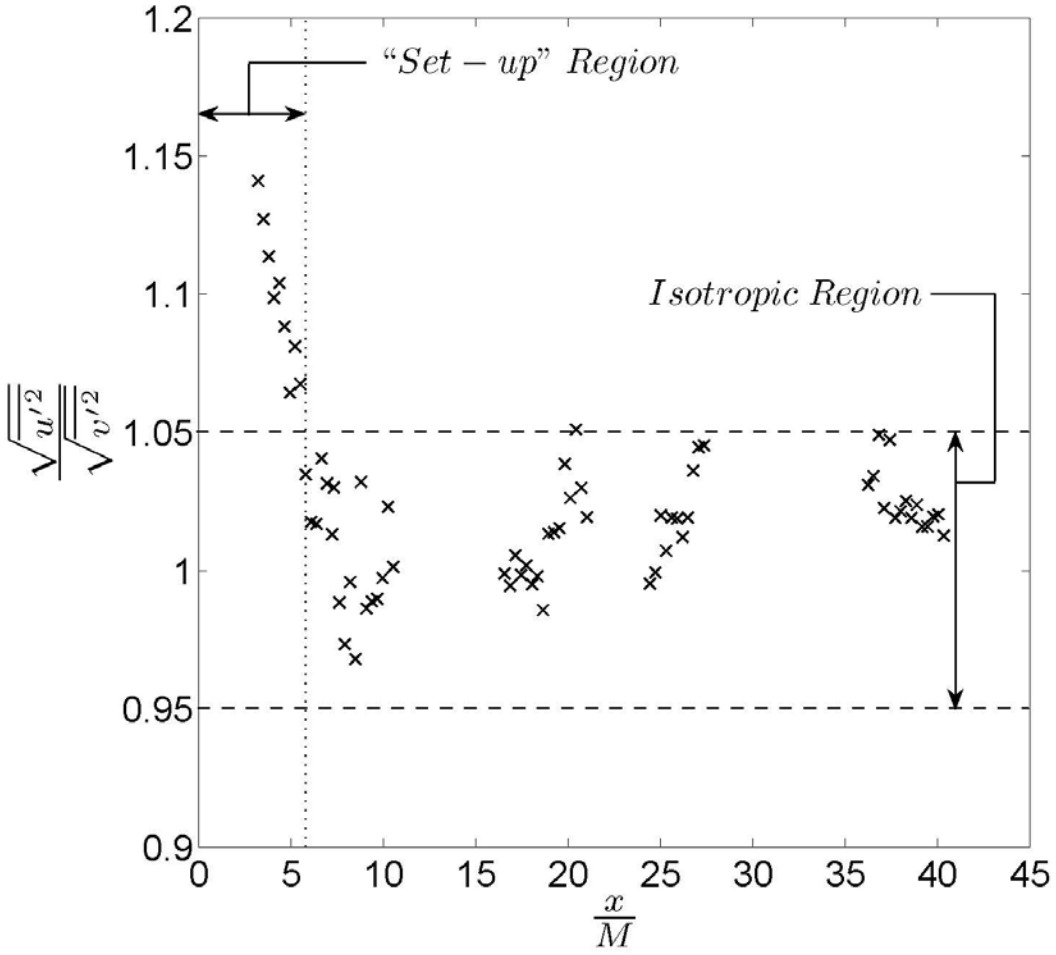

Figure 4.1. Evolution of the ratio of the streamwise and vertical velocity rms for the medium grid experiment, illustrating the anisotropic region closer to the grid. Every other PIV measurement is shown.

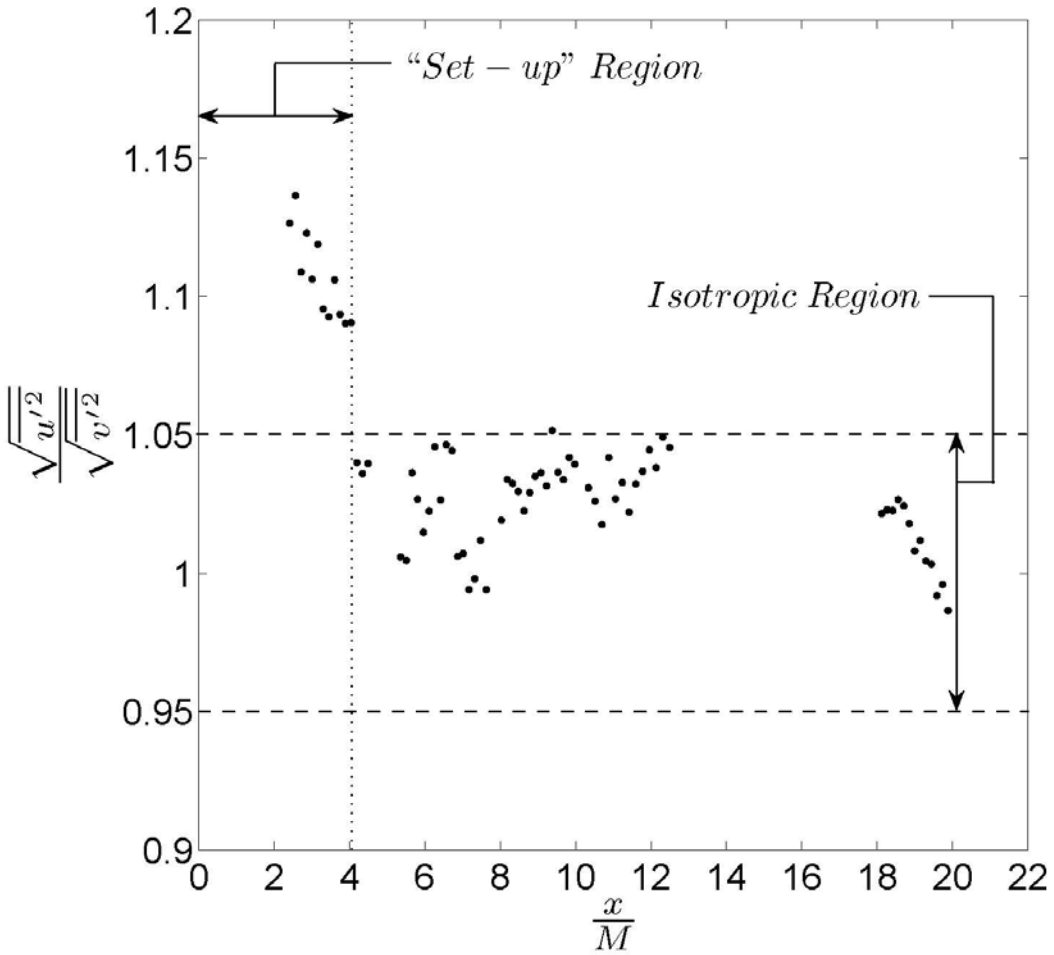

Figure 4.2. Evolution of the ratio of the streamwise and vertical velocity rms for the coarse grid experiment, illustrating the anisotropic region closer to the grid. Every other PIV measurement is shown.

several initial conditions have been measured for initialization of the model. The parameters necessary to describe the initial conditions present in the experiments of the current study include: the isotropic decay exponent for the grid turbulence (n), the turbulent kinetic energy ($\overline{K_{GT}}$) and the turbulent length scale ($\overline{S}$), which are defined in *4.3.2, 4.3.2,* and *4.3.3*, respectively. Measurements of the initial conditions for the medium and coarse grids were made using the PIV diagnostic described in *2.2.1*. Measurements of these parameters are discussed next.

4.2.1 Isotropic decay exponent

When the production of turbulent kinetic energy downstream of a grid ceases, the turbulent kinetic energy decays due to the cascade of energy from one wave number to another (Mohamed and LaRue 1990). The decay of grid-generated turbulence has been extensively investigated in wind tunnel experiments equipped with various types of grids using hot-wire anemometry. According to Pope (2000), the turbulent kinetic energy and normal stresses of grid-generated turbulence decay as a power law which is defined as Equation (1.4) in *1.1.4*. Because the turbulence generated by the grids in the current study is shown to be isotropic in *4.3.1*, and PIV is a two-dimensional measurement, the turbulent kinetic energy measurement at each point is a time-average as well a spatial average over approximately 2 *cm* in the y direction. For traditional grid-generated turbulence studies, the decay exponent, n, is evaluated over a large range of grid lengths, M, typically 10-50 $\leq x/M \leq$ 150, over which the flow is considered approximately isotropic. Because of facility restrictions, the range to measure the decay exponent in the current investigation is limited to $2 \leq x/M \leq$ 20-45, depending on the size of the grid. The approximately isotropic regime of the flow in the current investigation ranges from 6-40 grid lengths (x/M) for the medium grid, as seen in Figure 4.1, and 4-20 grid lengths for the coarse grid, as seen in Figure 4.2. The turbulent kinetic energy, $\overline{K_{GT}}$, has been normalized by the square of the mean

velocity, U_m^2, and plotted as a function of grid lengths downstream from the splitter plate. Because of the small range over which the decay exponent can be measured for the current study, a virtual origin, x_0, must be determined. The virtual origin accounts for the fact that the origin of the turbulent velocity fluctuation may not coincide with the physical location of the grid (Mohamed & LaRue 1990). Although it is reported by Mohamed & LaRue (1990) that the virtual origin should be set to zero if the decay exponent analysis is performed in the approximately isotropic regime of the flow, the virtual origin for the current investigation must be evaluated because of the comparably short range over which the decay exponent measurement can be performed. The decay exponent, n, from Equation (1.4) in *1.1.4* is evaluated by reformulating Equation (1.4) into Equation (4.2) (Mohamed & LaRue 1990).

$$\log\left(\frac{\overline{K_{GT}}}{U_m^2}\right) = \log(A) - (n)\log\left(\frac{x}{M} - \frac{x_0}{M}\right) \tag{4.2}$$

The method of least squares is used to determine the value of A and n, while the virtual origin, x_0, is evaluated by determining which virtual origin value gives the lowest error for the least squares fit (Comte-Bellot & Corrsin 1966). The virtual origins for the medium and coarse grids are 3.5 *cm* and 5.1 *cm*, respectively. The decay exponent (n) and the decay coefficient, A, for the medium grid are 1.44 ± 0.14 and 0.26 ± 0.12, respectively and for the coarse grid are 1.65 ± 0.11 and 0.29 ± 0.06, respectively. The decay of the turbulent kinetic energy for the medium and coarse gird experiments and the least squares fit for each are shown in Figure 4.3. The decay exponent, n, and decay coefficient, A, for both grids are larger than those measured in large grid Reynolds number wind tunnel experiments, which were approximately 1.3 and 0.02-0.1 (Mohamed and LaRue 1990; Sreenivasan *et al*. 1980). The difference for the decay exponents and decay coefficient between the current investigation and grid turbulence studies is likely due to the limited measurable range for the PIV, and for the increased solidity ratio of the current

grids. The decay exponent is used in the calculation of the isotropic decay constant necessary for the initialization of the BHR turbulent transport model. The isotropic decay constant for the BHR turbulent mix model is defined by Equation (4.3) (Pope 2000).

$$C_2 = \frac{n+1}{n} \tag{4.3}$$

Measurement of the isotropic decay constant ensures accurate modeling for the decay of the grid-generated isotropic turbulence present in the current investigation. The decay exponent, *n*, acquired from the medium and coarse grid experiments determine the corresponding isotropic decay constants using Equation (4.3). The isotropic decay constants to be used in the initialization of the BHR model for the medium and coarse grids are 1.69 ± 0.07 and 1.61 ± 0.04, respectively.

4.2.2 Turbulent kinetic energy

Another quantity necessary for initialization of the BHR turbulent transport model is the initial value of the turbulent kinetic energy. Previously, in *4.1*, the point at which the flow became isotropic was defined for the medium and coarse grids. Since the flow immediately following the grid is anisotropic, the initial value of the turbulent kinetic energy should also be defined at the point in which the turbulence becomes isotropic.

Since PIV is a two-dimensional measurement, the conventional definition for turbulent kinetic energy cannot be used in the form that involves all three velocity components. However, for grid turbulence in channel flow, the magnitudes of the span-wise velocity variance, $\overline{w'^2}$, and the vertical velocity variance, $\overline{v'^2}$, are assumed to be of similar magnitudes. Thus, the initial turbulent kinetic energy of the experimental outside the mixing layer is defined using Equation (4.4).

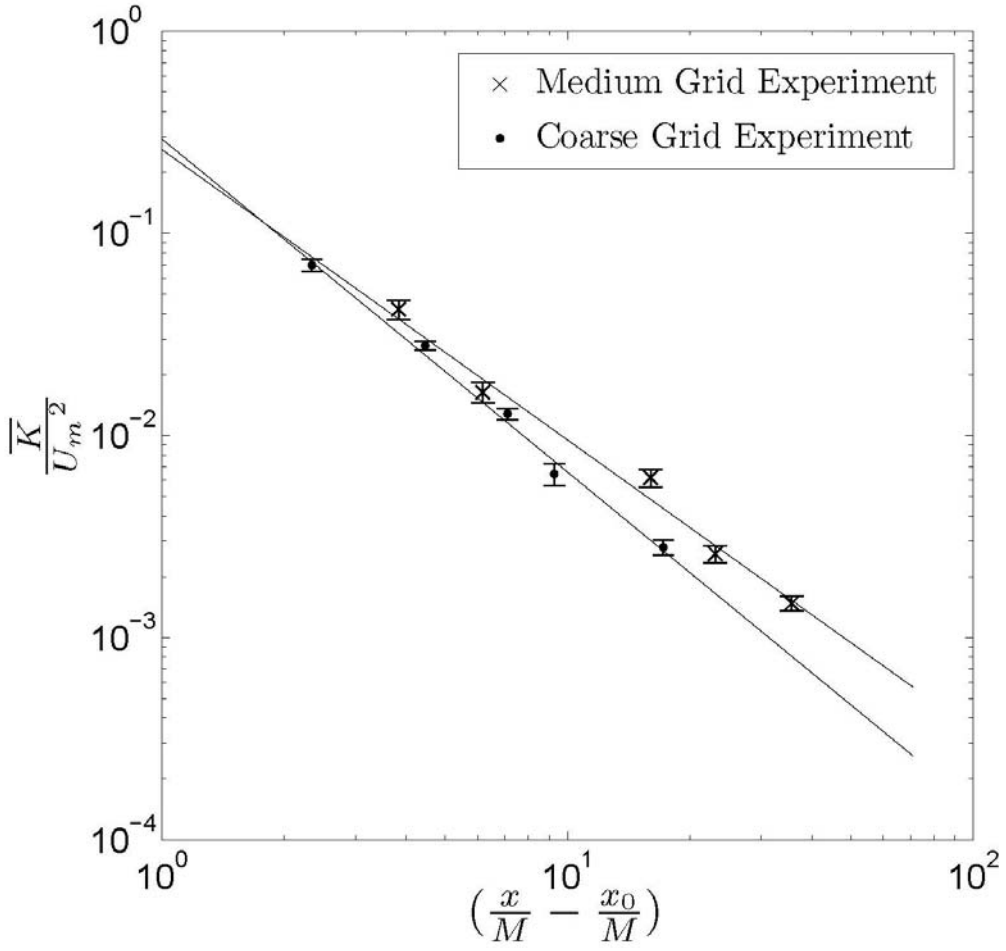

Figure 4.3. Power-law decay of the turbulent kinetic energy normalized by the square of the mean velocity and its error bars with the least squares fit for the medium (x) and coarse (·) grid experiments.

$$\overline{K_{GT}} = \frac{1}{2}\left(\overline{u'^2} + 2\overline{v'^2}\right) \tag{4.4}$$

It should also be noted that the turbulent kinetic energy within the Rayleigh-Taylor turbulent mixing layer is defined in Equation (4.5) where the span-wise velocity variance, $\overline{w'^2}$, is approximately equal to the stream-wise velocity variance, $\overline{u'^2}$.

$$\overline{K_{RT}} = \frac{1}{2}\left(2\overline{u'^2} + \overline{v'^2}\right) \tag{4.5}$$

Equation (4.5) is acceptable within the RT mixing layer based on the axisymmetry of the coherent structures (Ramaprabhu & Andrews 2004).

Figure 4.4 illustrates the decay of turbulent kinetic energy generated by the grids in the free stream, outside of the mixing layer, for the medium and coarse grid experimental setups. Every other PIV data point is shown in Figures 4.4 for clarity. Both free stream turbulent kinetic energies, $\overline{K_{GT}}$, for the medium and coarse grids were calculated using Equation (4.4). For the medium grid, the initial value for the turbulent kinetic energy is 1.12 ± 0.10 cm^2/s^2 when the flow is defined to be isotropic (approximately four grid lengths downstream from the splitter plate). For the coarse grid, the initial value for the turbulent kinetic energy is 1.82 ± 0.13 cm^2/s^2 when the flow is defined to be isotropic (approximately six grid lengths downstream from the splitter plate). Initial values for the turbulent kinetic energy for both the medium and the coarse grids can now be used to initialize the BHR turbulent transport model.

4.2.3 Turbulent length scale

A final initialization parameter necessary for the BHR turbulent transport model is the turbulent length scale, $\overline{S}$. There are several definitions of length scales in turbulence. There are length scales to define the largest eddies as well as the length scales to define the smallest eddies.

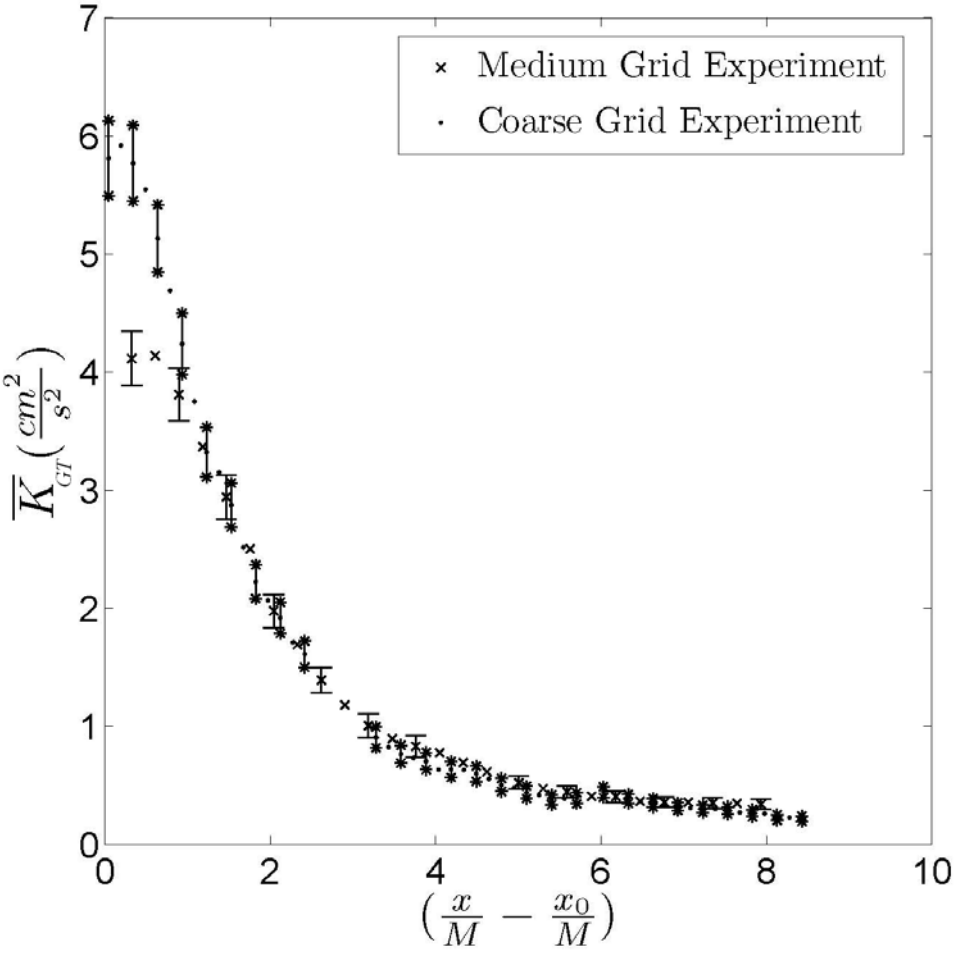

Figure 4.4. Evolution of turbulent kinetic energy for the medium grid (x) and coarse grid (·) experimental setup. Every other PIV data point is shown. Error bars for the medium grid (-) and the coarse grid (*) are shown approximately every fourth point.

The length scale definition adopted for the current application is the length scale characterizing the large eddies. Before identifying the turbulent length scale used for this study, it is necessary to discuss the manner in which the dissipation term, ε, is determined. For decaying isotropic turbulence, dissipation can be described as the time rate of change of the free stream turbulent kinetic energy, defined in Equation (4.6), where $dt=-dx/U_m$ according to Taylor's hypothesis (Pope 2000).

$$\frac{d\overline{K_{GT}}}{dt} = -\varepsilon \tag{4.6}$$

The dissipation term in Equation (4.6) was obtained from performing a least-squares fit on the decay of $\overline{K_{GT}}$ over a short period of evolution, approximately 0.15 *s*, to capture the initial magnitude of the dissipation of turbulence kinetic energy. The initial values for dissipation for the medium and coarse grids are 1.44 ± 0.06 and 1.69 ± 0.06 cm^2/s^3, respectively. Once the flow is considered isotropic, the initial turbulent length scale is defined by Equation (4.7) (Pope 2000), where $\overline{K_{GT}}$ is the initial value for the turbulent kinetic energy defined in *4.3.2*.

$$\overline{S} \equiv \frac{\overline{K_{GT}}^{3/2}}{\varepsilon} \tag{4.7}$$

Using the initial value of the turbulent kinetic energy and the initial value for dissipation discussed previously, the initial turbulent length scale for the medium grid is 0.83 ± 0.12 *cm*, at *x/M*=6, and 1.46 ± 0.17 *cm*, at *x/M*=4, for the coarse grid. The measured turbulent length scales are of the same order as the rod diameters for the medium and coarse grids. This similarity of magnitudes is due to the larger length scales being introduced to the flow by the vortices shed from the rods. A summary of the measured initial conditions to be used for the initialization of the BHR turbulent transport model are found in Table 4.1.

4.3 Performance evaluation of the BHR turbulent transport model

Initial values for the turbulent kinetic energy, the turbulent length scale and the isotropic decay exponent have been experimentally measured for the medium and coarse grid setups in the Texas A&M water channel facility. Two turbulent quantities are compared between the model and the water channel experiments. The self-similar growth parameter, α, from the model is compared with the experiment to determine if the model is able to describe the difference in the self-similar behavior that has been shown in the medium and coarse grid experiments. The self-similar growth parameter of the turbulent kinetic energy, α_K, from the model is also compared with the experiment to determine how well the model describes the turbulent kinetic energy generated by the grid and the RT mixing layer. Before the performance of the BHR turbulent transport model is evaluated, initialization of the model is discussed.

The RAGE (Radiation Adaptive Grid Eulerian) hydro-code (Gittings *et al.* 2006) is set to one-dimensional Cartesian geometry with the two materials defined such that the higher density material is defined for a region above the interface, and the lower density material is defined for a region below the interface. The densities of the materials are set to define an Atwood number of 0.04. The Atwood number for the model is slightly higher than the experimental values (0.0005-0.00075) to decrease computational cost. Also, scaling laws for RT indicate that α and α_K are proportional to the Atwood number, for small Atwood numbers, thus the value of 10^{-4} and 0.04 may be used as long as A_t scaling is applied. The height of the domain is 200 *cm* and the width of the domain is 2 *cm*. The model is initialized with the set of measured initial conditions from the medium and coarse grid experiments and run for four seconds. The initial conditions values for the medium and coarse grid experiment are found in Table 4.1. The values of the model constants used for the current investigation for the medium and coarse grid are summarized in Table 4.2. The only two model constants altered for the current study are the

isotropic decay constant, *C2*, and the weighting constant for the length scale transport equation, *C4*. The previous value of the isotropic decay constant, *C2*, was 1.92, which, using Equation (4.3), gives a value of 1.09 for the isotropic decay exponent, *n*. Since a unique isotropic decay exponent is determined for the medium and coarse grid experiments, the value of *C2* is changed to reflect the experimental measurements. The model constant, *C4*, is increased from a value of 0.65 to the values shown in Table 4.2 for the medium and coarse grid model runs. By increasing the magnitude of *C4*, the turbulent mass flux decreases and thus the growth of the mixing layer is decreased. The remaining parameters in Table 4.2 were obtained through a private communication with Gore (Gore 2007).

The growth parameter, α, is evaluated using the method described in *3.2.3* for the experimental evaluation of the growth parameter. Figure 4.5 shows the non-dimensional evolution of the mixing layer height from which the growth parameter can be evaluated for both the model and the experiment. The growth parameters evaluated from the model when initialized with the medium and coarse grid parameters are 0.063 and 0.060, respectively. Looking at Figure 4.5, the experimentally measured and the modeled development of the mixing layer height compare well with the exception of the magnitude of the non-dimensional height, which is caused by a diffuse interface setup by the grids for the medium and coarse grid experiments that is not defined in the model. The height of the mixing layer immediately following the splitter plate is not able to be measured because of interference from the grid. Therefore, the initial height of the mixing layer at t=0 cannot be measured. Comparing the growth parameter of the experiments and the model from Figure 4.5, when initialized with unique initial conditions from the medium and coarse grid experiments, provides evidence that the BHR turbulent transport model, when initialized correctly, does capture the change in the growth parameter for the penetration height of the spikes/bubbles for the self-similar regime of

Parameters	Turbulent Kinetic Energy $\overline{K_{GT}}$ (cm^2/s^2)	Turbulent Length Scale $\overline{S}$ (cm)	Isotropic Decay Constant $C2$
Medium Grid	1.12	0.83	1.69
Coarse Grid	1.82	1.46	1.61

Table 4.1. Measured initial conditions for the medium and coarse grid experimental setups necessary for initialization of the BHR turbulent transport model.

Parameter	Medium Grid	Coarse Grid
C1	1.44	1.44
*C2	1.69	1.61
C3	0.00	0.00
*C4	0.69	0.71
Ca1	7.00	7.00
Ca2	0.25	0.25
C_μ	0.28	0.28
σ_ε	0.10	0.10
σ_c	0.60	0.60
σ_{sie}	1.00	1.00

Table 4.2. Initialization values of model constants for the BHR turbulent transport model.

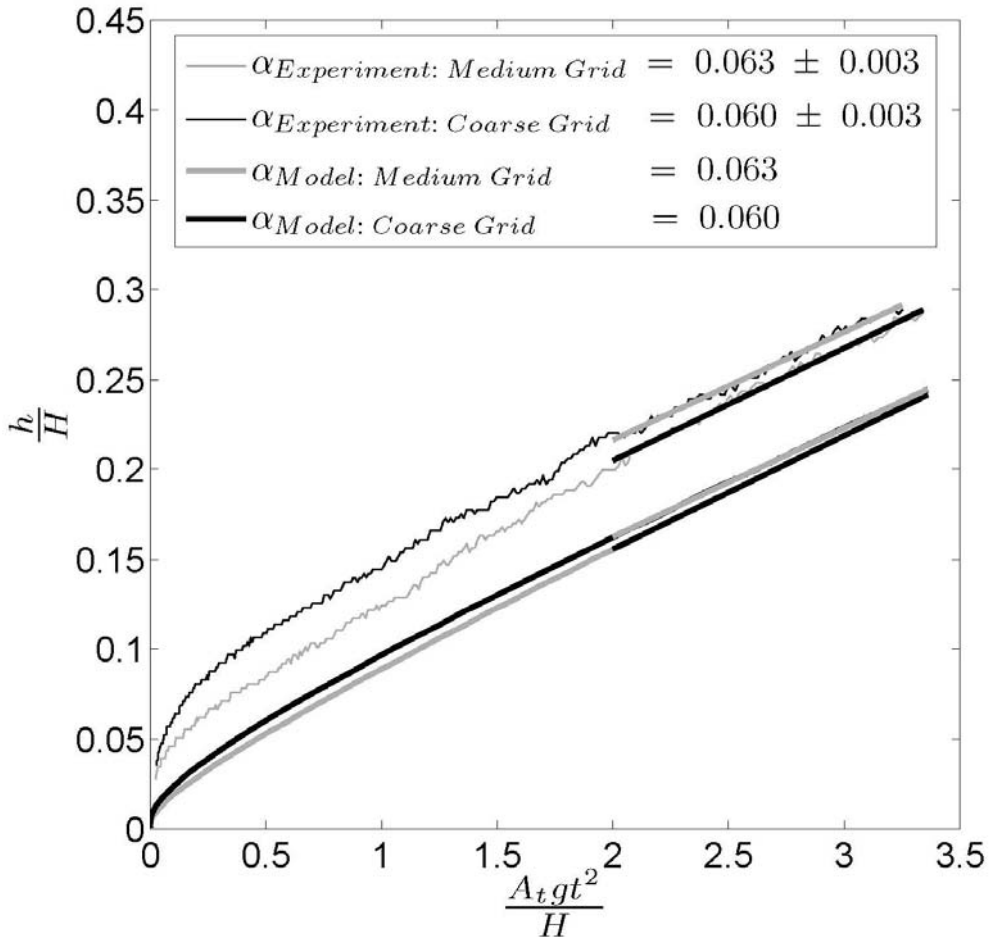

Figure 4.5. Non-dimensional evolution of the mixing layer height for the model initialized with the measured initial conditions from the medium and coarse grid experimental setups. The experimental non-dimensional evolution of the mixing layer height for the medium and coarse grid setups have been plotted for comparison.

the flow. A summary of the experimental and modeled growth parameters is given in Table 4.3.

Another turbulent quantity used to evaluate the performance of the model is the turbulent kinetic energy at the centerline of the mixing layer. To compare the turbulent kinetic energy from the experiment and the model, measurements are taken of the centerline turbulent kinetic energy for the medium and coarse grid experiments. The experimental turbulent kinetic energy, $\overline{K_{RT}}$, at the centerline of the mixing layer is defined using Equation (4.5) in *4.3.2*, and again as $\overline{K_{RT}} = 1/2\left(2\overline{u'^2} + \overline{v'^2}\right)$.

Analogous to the measurement of the growth parameter for the height of the mixing layer, α, a growth parameter for the turbulent kinetic energy, α_K, is desirable to compare the model with the present experiments. A relation for the growth of the centerline turbulent kinetic energy, $\overline{K_{RT}}$, is defined in Equation (4.8).

$$\overline{K_{RT}} = \alpha_K \left(A_t g t\right)^2 \tag{4.8}$$

Using $A_t g$ scaling, the centerline turbulent kinetic energy for the medium and coarse grid experiments as well as the model initialized with the medium and coarse grid initial conditions is plotted in Figure 4.6 as a function of $(A_t g t)^2$, where A_t is the Atwood number, g is the gravitational acceleration, and t is time ($t=x/U_m$ using Taylor's hypothesis). Figure 4.6 has been non-dimensionalized by the Atwood number, A_t, gravitational acceleration, g, and the height of the domain, H. To compare the behavior self-similar portion of the flow, which is defined as $(A_t g t)^2/(A_t g H) \approx$ 1.75-2.75, between the experiment and the model, a least squares fit is performed to obtain a measure of $d\overline{K_{RT}}/d\left(A_t g t\right)^2$ and the slope provides a measure of α_K. Obtaining the growth parameter of the turbulent kinetic energy, α_K, from the self-similar portion of the experimental data in Figure 4.6 yields a value of 0.0119 ± 0.006 for the medium

	α (Experiment)	α (Model)
Medium Grid	0.063 ± 0.003	0.063
Coarse Grid	0.060 ± 0.003	0.060

Table 4.3. Experimentally measured and BHR modeled α .

grid and 0.0129 ± 0.006 for the coarse grid. Similarly, the growth parameter for the turbulent kinetic energy from the self-similar portion of the flow for the model with the medium grid initial conditions is 0.0091 and 0.0088 for the model with the coarse grid initial conditions.

Table 4.4 provides a comparison of the experimentally measured and modeled growth parameter for the turbulent kinetic energy at the centerline. The model does fall within the uncertainty of the measurement for the medium and coarse grid comparisons. Since the objective of the current investigation is to compare the self-similar results between the BHR model and the experiment, the discrepancy in magnitudes of the development of turbulent kinetic energy in Figure 4.6 was not addressed. The discrepancy is present because the BHR model is initialized with the measured turbulent kinetic energy of the grid-generated turbulence (i.e. outside the mixing layer) when the flow became isotropic. Because RT instabilities (i.e. the height of the mixing layer) grow by converting potential energy of the mean flow into kinetic energy, the turbulent kinetic energy of the mixing layer begins to grow immediately after the grids (Kraft, 2008). The turbulent kinetic energy value used in the initialization of the BHR model did not take into account the turbulent kinetic energy generated from the release of potential energy within the RT mixing layer before the flow became isotropic.

Since the growth parameter, α, of the turbulent mixing layer describes the growth of the mixing layer, and the growth of the mixing layer is directly related to the production of kinetic energy within the mixing layer, the growth parameter, α_K, of the turbulent kinetic energy in the self-similar region of the mixing layer should be proportional to the behavior of the growth parameter, α, of the penetration height. For the current investigation, it was shown in *3.2.3* that the growth parameter of the mixing layer penetration height decreased between the medium and the coarse grid experiments. The same decreasing trend is not clearly seen from the growth parameter of the turbulent kinetic energy, α_K, at the centerline of the mixing layer between the

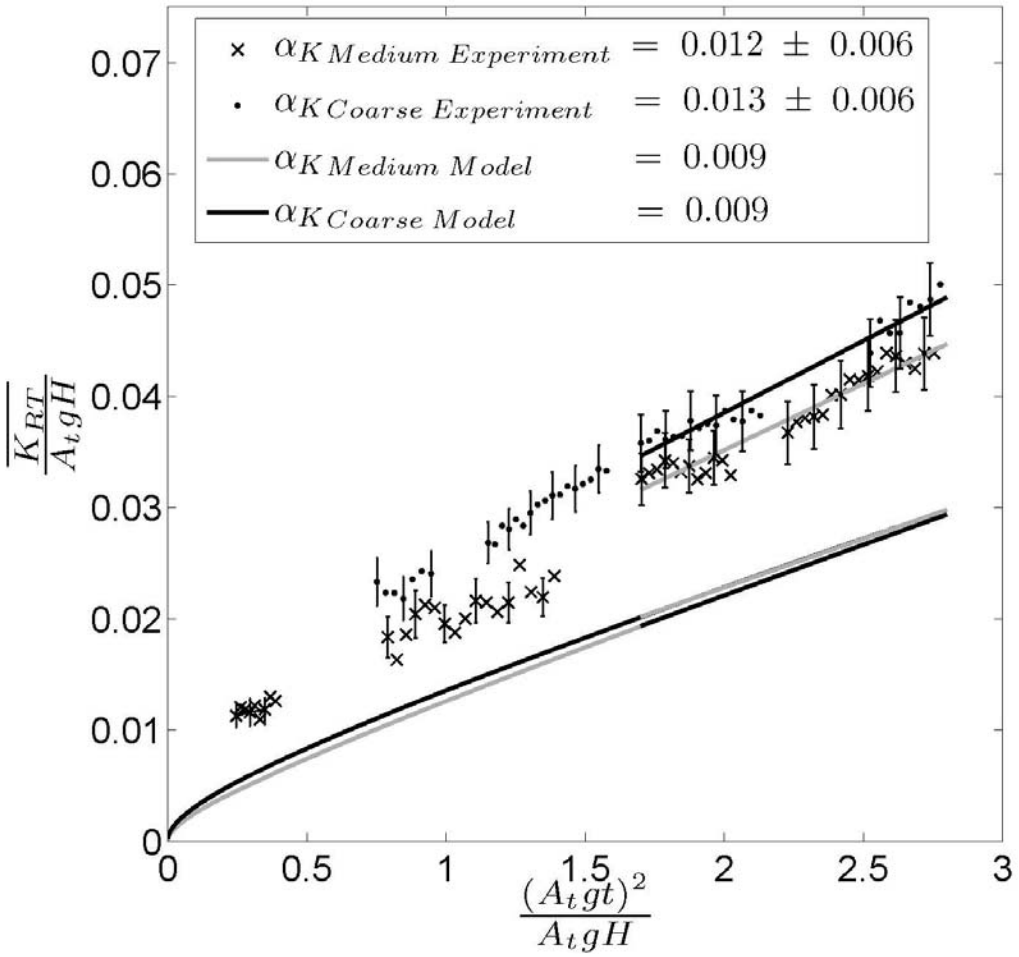

Figure 4.6. - Evolution of the centerline turbulent kinetic energy for the medium (x) and the coarse (·) grid experiments and the model initialized with the initial conditions of the medium and coarse grid experiments. Every other PIV data point is shown and the error bar for every sixth data point is shown on both the medium and the coarse grid data points.

	α_K (Experiment)	α_K (BHR)
Medium Grid	0.0119 ± 0.006	0.0091
Coarse Grid	0.0129 ± 0.006	0.0088

Table 4.4. Experimentally measured and BHR modeled α_K .

medium and coarse grid experiments. However, for the model, when initialized with the initial conditions from the medium grid experiment, a slight decrease is seen in the growth of the turbulent kinetic energy when compared to the model initialized with the coarse grid initial conditions.

The performance of the BHR turbulent transport model has been evaluated by comparing the growth of the penetration height and the growth of the turbulent kinetic energy at the centerline of the mixing layer for the model initialized with the initial conditions measured in the medium and coarse grid experiments. The self-similar growth of the penetration height of the mixing layer was described accurately by the BHR model when initialized with the measured initial conditions for each. The decrease in the growth parameter, α, from the medium grid experiment to the coarse grid experiment was observed in the results of the model. The growth parameter of the centerline turbulent kinetic energy, α_K, measured from the model results exhibited a decreasing trend between the medium and coarse grid initialized models, similar to the growth parameter of the penetration height, α. The model results for the growth parameter of the centerline turbulent kinetic energy, α_K, fell within the uncertainty of the experimentally measured growth parameters. Overall the BHR model, when initialized with unique, experimentally measured initial conditions, captures the self-similar behavior of the turbulent mixing layer.

5. SUMMARY, CONCLUSIONS, AND FUTURE WORK

An experimental investigation about the effects of initial conditions on a buoyancy-driven Rayleigh-Taylor mixing layer has been conducted in a water channel facility at Texas A&M University. The facility orients cold water above hot water to form an unstable stratification which promotes the formation of a turbulent mixing layer. The statistically steady quality of the experiment provides the necessary environment to enable turbulence statistics to be experimentally evaluated. The experimental investigation of different initial conditions was performed to determine if a change in the behavior of the mixing layer occurs, and to provide necessary initialization parameters for the performance evaluation of the BHR turbulent transport model.

Conclusions of the present study have been divided into two groups based on the two objectives of the investigation.

Objective 1 - To determine if the late-time development of a low Atwood number buoyancy driven RT mixing layer can be altered by changing the initial conditions.

- A change in the initial conditions was accomplished by positioning a bi-planar stationary grid, made up of cylindrical rods, immediately downstream from the termination of the splitter plate.
- When the larger grids were placed immediately downstream from the termination of the splitter plate, a change in the dynamics of the initial mixing layer was qualitatively observed.
- Performing a quantitative measurement of the height of the mixing layer for all three initial conditions using a calibrated visualization technique

yielded a change in the self-similar growth parameter, α, from 0.072 ± 0.03 for the fine grid to 0.063 ± 0.003 and 0.060 ± 0.003 for the medium and coarse grids, respectively.

Objective 2 - To experimentally measure turbulence statistics of a low Atwood number buoyancy-driven RT mixing layer to provide an experimental data set for use in a performance evaluation and validation efforts for the BHR turbulent transport model.

- Generation of approximately isotropic grid turbulence was verified for the medium and coarse grids.
- Measurements of the isotropic decay exponent, *n*, the turbulent kinetic energy, $\overline{K_{GT}}$, and the turbulent length scale, $\overline{S}$, were experimentally obtained for the medium and coarse grids to define the initial conditions necessary for the accurate initialization of the BHR turbulent transport model.
- A performance evaluation of the BHR turbulent transport model was performed and agreement was found between the growth parameters, α and α_K of the experiment and the model, when initialized with accurate initial condition values.

Upon completing this study, several opportunities for future work were revealed. Several areas that could be addressed in a future investigation include:

- Investigate the influence of grid solidity, σ, rod geometry and rod diameter on the grid-generated turbulence and the development of the RT mixing layer.

- Perform a spectral investigation of the evolution of density fluctuations along the centerline of the mixing layer to provide another evaluation parameter for the BHR turbulent transport model.
- Increase or decrease the rod size (try to generate an even broader range of initial wavelengths) to determine if a lower growth parameter, α, can be experimentally measured.
- Investigate whether or not molecular mixing is affected by initial conditions, and whether the BHR turbulent transport model can accurately describe the experiments.
- Determine if the BHR turbulent transport model can describe the "set-up" region of the grid-generated turbulence.

REFERENCES

Andrews, M. J. & Spalding, D. B. 1990 A simple experiment to investigate two-dimensional mixing by Rayleigh-Taylor instability. *Phys. Fluids A* **2**, 922-927.

Banerjee, A. 2006 Statistically steady measurements of Rayleigh-Taylor mixing in a gas channel. PhD Dissertation, Texas A&M University, College Station.

Batchelor, G. K. & Townsend, A. A. 1948*a* Decay of isotropic turbulence in the initial period. *Proc. Roy. Soc. A* **193**, 539-558.

Benedict, L. H. & Gould, R. D. 1996 Towards better uncertainty estimates for turbulence statistics. *Exps. Fluids* **22**, 129-136.

Besnard, D., Harlow, F. H. & Rauenzahn, R. M. 1987 Conservation and transport properties of turbulence with large density variations. *Los Alamos National Laboratory Report*, LA-10911-MS

Besnard, D., Harlow, F. H., Rauenzahn, R. M. & Zemach, C. 1992 Turbulence transport equations for variable-density turbulence and their relationship to two-field models. *Los Alamos National Laboratory Report*, LA-12303-MS.

Chandrasekhar, S. 1961 *Hydrodynamic and Hydromagnetic Stability*. New York: Dover.

Comte-Bellot, G. & Corrsin, S. 1966 The use of a contraction to improve the isotropy of grid-generated turbulence. *J. Fluid Mech.* **25**, 657-682.

Cook, A. W. & Dimotakis, P. E. 2001 Transition stages of Rayleigh-Taylor instability between miscible fluids. *J. Fluid Mech.* **443**, 69-99.

Dimonte, G. & Schneider, M. 1996 Turbulent Rayleigh-Taylor experiments with variable acceleration. *Phys. Rev.* E **54**, 3740-3743.

Gad-el-hak, M. & Corrsin, S. 1974 Measurements of nearly isotropic turbulence behind a uniform jet grid. *J. Fluid Mech.* **62**, 115-143.

Gittings, M., Weaver, R., Clover, M., Betlach, T., Byrne, N., Coker, R., Dendy, E., Hueckstaedt, R., New, K., Oakes, W. R., Ranta, D. & Stefan, R. 2006 The RAGE radiation-hydrodynamic code. *Los Alamos National Laboratory report*, LA-UR-06-0027.

Gore, R. 2007 Private communication on current values for BHR model constants. Los Alamos National Laboratory, Los Alamos.

Grue, J., Jensen, A., Rusas, P. & Sveen, J. K. 2000 Breaking and broadening of inertial waves. *J. Fluid Mech.* **413**, 181-217.

Gull, S. F. 1975 The X-ray, optical and radio properties of young supernova remnants. *Mon. Not. Roy. Astron. Soc.* **171**, 263-278.

Kline, S. J. & McClintock, F. A. 1953 Describing uncertainties in single-sample measurements. *Mech. Eng.* **75**, 3-8.

Kraft, W. N 2008 Simultaneous and instantaneous measurement of velocity and density in Rayleigh-Taylor mixing layers. Ph.D. Dissertation, Texas A&M University, College Station.

Kukulka, D. J. 1981 Thermodynamic and transport properties of pure and saline water. M.S. Thesis, State University of New York at Buffalo.

Lavoie, P., Burattini, P., Djenidi, L. & Antonia, R. A. 2005 Effect of initial conditions on decaying grid turbulence at low R_λ. *Exp. Fluids* **39**, 865-874.

Laws, E. M. & Livsey, J. L. 1978 Flow through screens. *Ann. Rev. Fluid Mech.* **10**, 247-266.

Lindl, J. 1995 Development of the indirect-drive approach to inertial confinement fusion and the target physics basis for ignition and gain. *Phys. Plasmas* **2**, 3933-4024.

Ling, S. C. & Huang, T. T. 1970 Decay of weak turbulence. *Phys. Fluids* **13**, 2912-2924.

Liu, R., Ting, D. S-K. & Rankin, G. W. 2004 On the generation of turbulence with a perforated plate. *Exp. Thermal and Fluid Sci.* **28**, 307-316.

Mohamed, M. S. & LaRue, J. C. 1990 The decay power law in grid-generated turbulence. *J. Fluid Mech.* **219**, 195-214.

Mueschke, N. J. 2004 An investigation of the influence of initial conditions on Rayleigh-Taylor mixing. M. S. Thesis, Texas A&M University, College Station.

Mueschke, N. J., Andrews, M. J. & Schilling, O. 2006 Experimental characterization of initial conditions and spatio-temporal evolution of a small-Atwood-number Rayleigh-Taylor mixing layer. *J. Fluid. Mech.* **567**, 27-63.

Mydlarski, L. & Warhaft, Z. 1996 On the onset of high-Reynolds-number grid-generated wind tunnel turbulence. *J. Fluid Mech.* **320**, 331-368.

Pope, S. B. 2000 *Turbulent Flows*. Cambridge, UK: Cambridge University Press.

Ramaprabhu, P. 2003 On the dynamics of Rayleigh-Taylor mixing. Ph.D. Dissertation, Texas A&M University, College Station.

Ramaprabhu, P. & Andrews, M. J. 2004 Experimental investigation of Rayleigh-Taylor mixing at small Atwood numbers. *J. Fluid Mech.* **502**, 233-271.

Read, K. I. 1984 Experimental investigation of turbulent mixing by Rayleigh-Taylor instability. *Physica* D **12** 45-58.

Roach, P. E. 1987 The generation of nearly isotropic turbulence by means of grids. *Int. J. Heat and Fluid Flow* **8**, 82-92.

Sharp, D. H. 1984 An overview of Rayleigh-Taylor instability. *Physica* D **12**, 3-18.

Simmons, L. F. G. & Salter, C. 1934 Experimental investigation and analysis of the velocity variations in turbulent flow. *Proc. Roy. Soc. A* **145**, 212-234.

Snider, D. M. & Andrews, M. J. 1994 Rayleigh-Taylor and shear driven mixing with an unstable thermal stratification. *Phys. Fluids* **6**, 3324-3334.

Sreenivasan, K. R., Tavoularis, S., Henery, R. & Corrsin, S. 1980 Temperature-fluctuations and scales in grid-generated turbulence. *J. Fluid Mech.* **100**, 597-621.

Steinkamp, M. J. 1996 Spectral analysis of the turbulent mixing of two fluids. Ph.D. Dissertation, University of Illinois at Urbana, Champaign.

Steinkamp, M. J., Gittings, M. L., Weaver, P. W. & Harlow, F. H. 2001 Implementation of a mix model into RAGE. *Los Alamos National Laboratory Report*, LA-UR-01-0572.

Taylor, G. I. 1935 Statistical theory of turbulence II. *Proc. Roy. Soc. Lon.* A **151**, 444-454.

White, C. M., Karpetis, A. N. & Sreenivasan, K. R. 2001 High-Reynolds-number turbulence in small apparatus: grid turbulence in cryogenic liquids. *J. Fluid Mech.* **452**, 189-197.

Wilson, P. N. & Andrews, M. J. 2002 Spectral measurements of Rayleigh-Taylor mixing at small Atwood number. *Phys. Fluids* **14**, 938-945.

Youngs, D. L. 1984 Numerical simulation of turbulent mixing by Rayleigh-Taylor instability. *Physica* D **12**, 32-44.

APPENDIX A

OPERATING PROCEDURES: WATER CHANNEL

1. a. Fill cold water tank by opening valve on the wall behind the water fountain. Increased filling speed can be accomplished by placing water hose in cold water tank and turning on (valve outside men's restroom)

   b. Fill hot water tank by opening building hot water valve under the sink in the men's restroom (key is kept in experiment room). Additional hot water can be obtained from the hot water heater in the room. Water from the hot water heater can be added to either tank by adjusting the corresponding valves.

2. Once the tanks are approximately half full, plug in sump pumps.
3. Make sure outlet plenum valves are closed and fill the channel either by turning on the motor of the cold water tank, or by placing the water hose in the inlet plenum.
4. Remove bubbles under the splitter plate by removing clear tape from holes in the splitter plate and using the water hose to guide the bubbles to the holes.
5. After the tanks are full check temperatures in both tanks and if satisfactory, record them, if not adjust the temperatures by adding hot or cold water.
6. Cover the channel with the Plexiglass plates and place weights on them.
7. Just before starting the experiment, unplug the sump pumps.
8. Start running the experiment by plugging in the pump motors from the hot and cold water tanks at the same time.
9. Open the necessary valves on the outlet plenum and check to see that the water level does not decrease. Valve positions that require partial opening are marked.
10. Check for shear between the two streams by injecting dye onto the splitter plate. If the blob of dye distorts under shear, adjust the rotameter valves accordingly.
11. Repeat step 10 until shear is eliminated.
12. Collect data.
13. Turn off the pump motors to both tanks and let the water in the channel drain.

Safety Precautions for the Water Channel Facility:

1. Never leave power cords lying on the floor.
2. If at any time the channel is about to overflow, decrease the flow speed of both streams by closing the rotameter valves, or unplug the pump motors for both tanks.
3. Except while filling the channel, the valves on the outlet plenum should remain open to the marked position.
4. The experimental facility should remain clean and free of clutter, with ample space to move around freely.
5. If there are leaks in the water channel facility, the area should be mopped and left to dry before running the experiment.

APPENDIX B

WEDGE CALIBRATION

The calibration method used in this experiment is described in detail in Snider and Andrews (1994) as well as Banerjee (2006). To establish this relationship, a calibration wedge is filled with marked fluid from the supply tank and placed in the test section of the channel. The internal dimensions of the wedge are 30.6 cm long, 11.7 cm high, and 14.0 cm wide at its widest point. A linear relationship between the pixel intensity and the dye concentration is set in each experiment, which allows the two dimensional average technique to be valid. The minimum intensity of the test section must be greater than 60 to ensure the linear relationship between the pixel intensity and the dye concentration. Figure B.1 shows the linear variation in concentration as a function of increasing wedge depth. The width of the wedge is only 14 cm at its deepest point, while the depth of the test section is 20 cm. Since the relationship between the intensity and the depth is linear, the minimum and maximum intensity values, approximately 70 and 220, respectively, in the experiment are extrapolated from the linear fit in Figure B.2. A relationship between the amount of exposure and its corresponding intensity is determined from the characteristic curve for the digital camera (Davis and Walters, 1922). Figure B.3 shows the characteristic curve for the digital camera on the ISO 100 setting. For Figure B.3, the exposure is defined as LOG(Shutter Speed). The linear range for the intensity is approximately 65-245. From the linear range of intensity for the camera and the linear range of intensity for the dye, the linear range of intensity for current experiments must be set between 65 (darkest) and 245 (lightest). For current experiments, the intensity range was set to approximately 70-220.

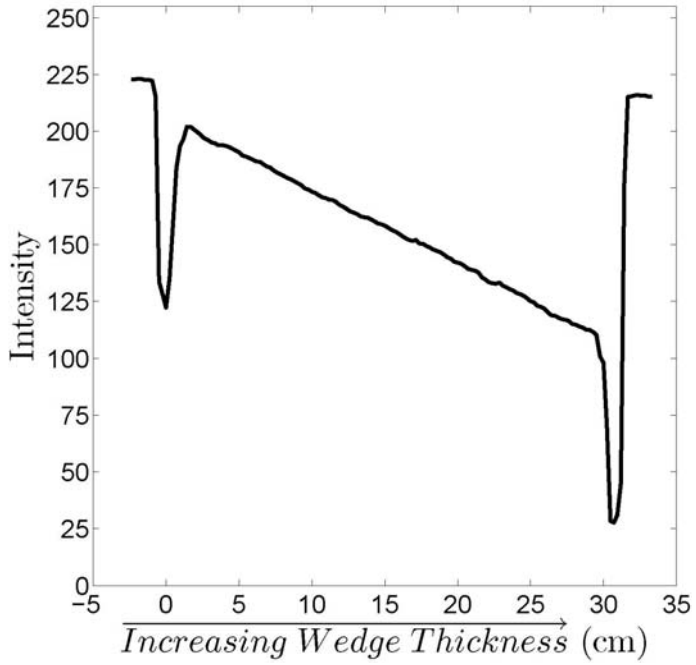

Figure B.1. Measured light intensity as a function of increasing wedge thickness.

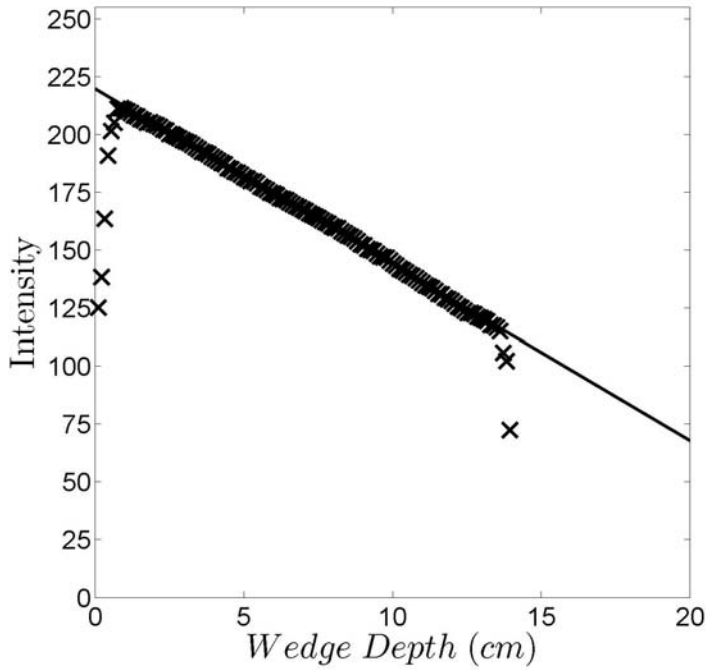

Figure B.2. Measured light intensity linearly extrapolated to the width of the channel.

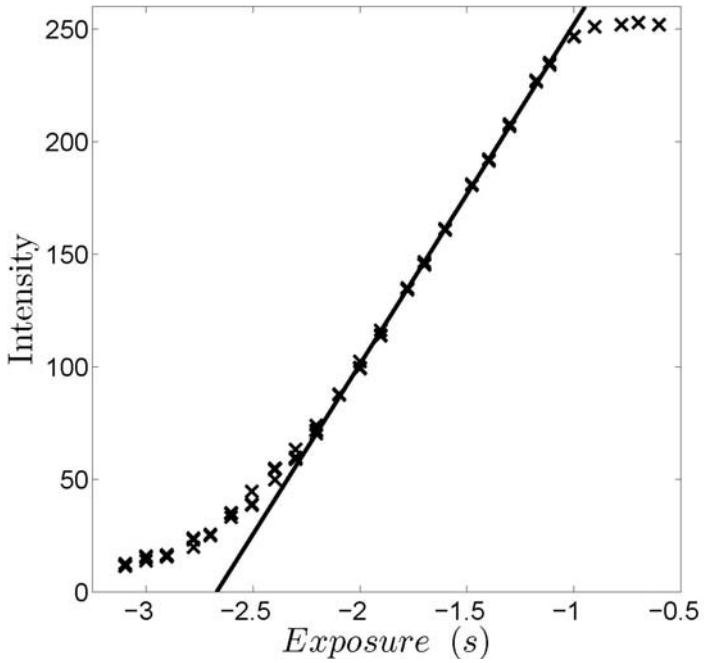

Figure B.3. Characteristic curve for the Canon A80 digital camera on the ISO 100 setting.

APPENDIX C

GROWTH PARAMETER MEASUREMENT: ORIENTATION 2

A set of image analysis experiments were performed with the medium and coarse grids at the termination of the splitter plate in the orientation 2 to determine if a change in the growth parameter, α, occurs with a variation in the orientation of the grids. Positioning the grids to orientation 2 is thought to further aid in destroying the boundary layers that form on the splitter plate. A small change in the growth parameter was found when the grids were positioned in orientation 2. Previously, with the grids positioned in orientation 1, the growth parameters for the medium and coarse grids were found to be 0.063 ± 0.003 and 0.061 ± 0.003, respectively. Looking at Figure C.1, the new growth parameters for the medium and coarse grids positioned in orientation 2 were found to be 0.060 ± 0.003 and 0.057 ± 0.003, respectively.

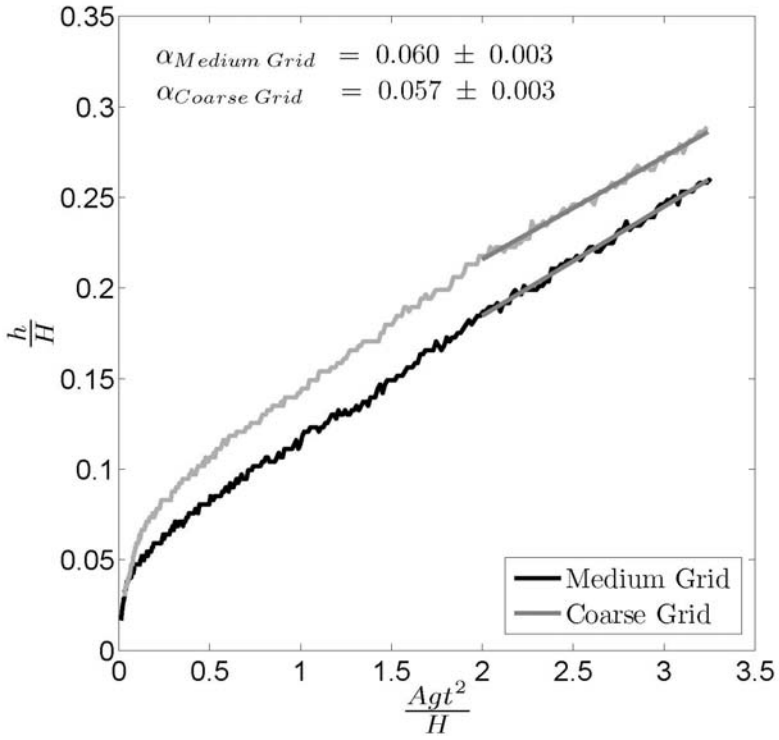

Figure C.1. Mixing layer half-width as a function of $A_t gt^2$ for the two separate experiments, one with the medium grid and another with the coarse grid placed immediately following the termination of the splitter plate in orientation 2, shown in Figure 2.1. Plot is non-dimensionalized by the channel height, *H*.

APPENDIX D

OPERATING PROCEDURES: PIV EXPERIMENTS

1. Follow steps 1-5 in the water channel experiment SOP (Appendix X).
2. While tanks are filling access PIV diagnostic equipment including: PIV computer, KODAK digital camera, PIV seed particles, PIV laser interlock keys, safety goggles and PIV laser system.
3. Put on Alignment Safety Goggles.
4. Align the laser head with the first directing mirror of the optics setup.
5. Check to ensure that the shutter is closed on the laser head.
6. Check to ensure the laser power settings are set to the lowest power level.
7. Insert the laser interlock keys and unlock the lasers
8. Plug power strip for lasers into electrical outlet on the far wall, next to the SOP bin and laser goggles.
9. Turn on the switch to power the electrical outlet discussed in step 3 for the laser power supplies and the "Laser in Use" warning light outside the door.
10. Turn on the power switches for the laser power supplies, which are located on the back of the laser power supplies.
11. Set the lasers to fire on the command of the "internal" trigger, which is controlled by the switch on the back of the laser power supplies. (Note: "Flash Lamp" switch is also located on the back of the laser power supply)
12. Ensure that the lasers are on "Standby" mode.
13. Allow laser to warm up for approximately fifteen minutes before beginning alignment.
14. Make sure sump pumps are on for both tanks and measure out necessary amount of seeding particles and mix with small amount of water then pour mixture into one tank.
15. Repeat step 13 for the remaining tank.
16. Place Plexiglass plates on top of channel and put weights on them.
17. Remove black, wooden cover from the front of the channel.
18. Align the optics system using the following steps (NOTE: for the alignment process, use only ONE laser):
    a. With the alignment safety goggles on, open the shutter on the laser head.

b. When ready, fire the laser using the "Fire" button on the control pad, and adjust the laser power level to the ideal power level for alignment (usually just past half way).
c. Since the laser beam is not visible, a piece of ORANGE paper should be used to visualize the location of the beam on each optic surface.
d. The beam should be incident at the center of each of the first two mirrors.
e. For the next two lenses, the beam should pass through the center of curvature.
f. The final lens is used to focus the laser sheet. The oblong beam incident on the final lens should also pass through the center of curvature of the lens.
g. In addition the laser sheet should be parallel to the flow direction for measurement of streamwise velocities. Focusing the laser sheet is accomplished by raising and lowering the final lens. A piece of ORANGE paper can be inserted underneath the channel to visualize the laser sheet. Focus the laser sheet on the bottom surface of the channel until the sheet is as thin as possible. Then slightly defocus the sheet by slowly lowering the lens until the sheet is approximately 0.5 *mm* thick. By doing this, the focal point of the laser sheet will be in the lower half of the channel instead of being focused on the bottom of the channel, which damages the Plexiglass. As a result, the laser sheet should diverge less prior to the measurement window.
h. The final result should be a laser sheet of approximately 1.0 *mm* thick in the measurement window. Also, the laser sheet should propagate perfectly vertical.

19. When finished aligning the optics, set the laser power level to its lowest setting.
20. Stop the laser from firing by returning the laser to the "Stop" position.
21. Close the shutter on the laser head.
22. Now that the lasers are in the "Stop" position and ***CANNOT*** energize, put on the 5+ OD Safety Goggles.
23. Place black, wooden cover back in front of the channel.
24. Set up the KODAK digital camera on the tripod and connect it to the PIV computer and the Pulse Generator.
25. Check to make sure the laser power settings are set to their lowest level.
26. Set each laser to "Standby" mode.
27. Power on the PIV Computer and when ready initiate the capture program ("11Jan2000" LabVIEW shortcut on the desktop).
28. Inside the LabVIEW interface, set the "Trigger" settings to disabled and RSTline0.

29. Enter the desired directory to save the images.
30. Execute a Test Capture prior to starting the signal generator.
31. Open the “HLGrab” shortcut on the desktop.
32. Turn on the Signal Generator and start the Triggering Program. (Refer to the Signal Generator SOP).
33. Turn off main laboratory lights.
34. Adjust Plexiglass plate and pour a small amount of the PIV seed solution into the channel in the approximate location of the laser sheet.
35. Using the continuous feed from the PIV digital camera (HLGrab interface) adjust the focus and the size and location of the interrogation window.
36. Turn power level of each laser up to approximately alignment power or slightly higher to illuminate the seed particles.
37. Capture several images from the PIV digital camera using the capture program opened in step 24.
38. Check the images to verify proper alignment of the optics (Since the particles are stationary, images captured using each laser should appear the same if the alignment was performed correctly).
39. Stop firing the lasers by stopping the Triggering program on the signal generator.
40. Set the laser power levels to their lowest settings.
41. Proceed with steps 6-11 from the Water Channel Experiment SOP.
42. When ready to capture PIV, restart the “Triggering Program” on the signal generator.
43. Adjust the power levels on each laser until they are matched. Use LabVIEW capture interface to check power level match.
44. Capture Images. (Usually 1200 images at 30 Hz for 640x480 resolution).
45. When finished, set the laser power levels to their lowest settings.
46. Stop the lasers from firing by returning the lasers to the “Stop” position.
47. Stop the Triggering Program on the signal generator.
48. Turn off pumps and shut exit plenum drain valves.
49. Use capture program to record a reference image for post-processing use.
50. Close the shutter on the laser head.
51. Turn the power supplies for both lasers off.
52. Remove the laser interlock keys from the laser power supplies.

53. Turn off the laser warning light.
54. Open exit plenum and allow channel to drain.
55. Cover all optics and replace PIV digital camera, PIV interlock keys, PIV seeding particles and PIV Safety Goggles to their storage location.
56. Replace optics system cover (black, wooden cover for the front of the channel).

APPENDIX E

OPERATING PROCEDURES: PULSE GENERATOR

1. Disconnect output and external trigger cables.
2. Turn on the pulse generator.
3. Reconnect output and external trigger cables.
4. Press “Function” then “Recall.”
5. Use next button to find Recall # 1, User: Lasers.
6. Press “Function” then “Recall” to load the settings.
7. With the camera on and connected to the PIV capture computer, open LabVIEW on the capture computer (“11Jan2000” Shortcut) and press the Run button on Labview Interface.
8. When ready to externally trigger lasers, return to the pulse generator and press “Run.”
9. When finished with the laser system, press “Run” to stop the pulse generator.

APPENDIX F

LOW-RESOLUTION (15 HZ) PIV VERIFICATION

A verification of the low-resolution PIV (15 Hz) experiments is needed to determine the validity of the experimental results. The low-resolution experiments were verified by post-processing the high-resolution PIV (30 Hz) experiments for the medium and coarse grids at 15 Hz, by post-processing alternate images rather than consecutive images. After reprocessing the experiments at 15 Hz, the centerline turbulent kinetic energies of the 30 Hz and 15 Hz were compared for the medium and coarse grid experiments.

The turbulent kinetic energy for the centerline of the mixing layer is larger in magnitude than that of the free stream. Therefore a comparison of the centerline turbulent kinetic energy for the medium and coarse grid will be performed. Looking at the turbulent kinetic energy at the centerline for the medium grid experiment in Figure F.1, the high-resolution and low-resolution data appear to collapse at approximately six mesh lengths (M) downstream from the splitter plate. The difference in the turbulent kinetic energies prior to six mesh lengths downstream of the end of the splitter plate is due to the larger magnitude of the span-wise, w', velocity component, which cannot be resolved by the low-resolution PIV.

An identical analysis was performed for the coarse grid PIV experiment. Looking at Figure F.2, the centerline turbulent kinetic energy from the coarse grid experiment processed at high-resolution and low-resolution do not collapse within the PIV interrogation window. However, an additional low-resolution experiment was performed further downstream and if the data from the first window was extrapolated, the high-resolution and low-resolution curves would collapse at approximately six mesh lengths downstream from the end of the splitter plate, similar to the medium grid experiment.

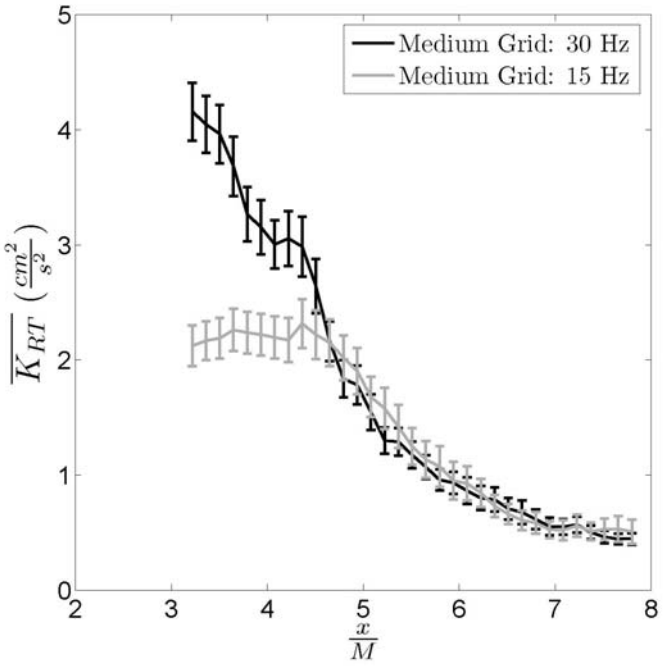

Figure F.1. Downstream evolution of centerline turbulent kinetic energy, with error bars, for the medium grid experiment processed at 15 and 30 Hz.

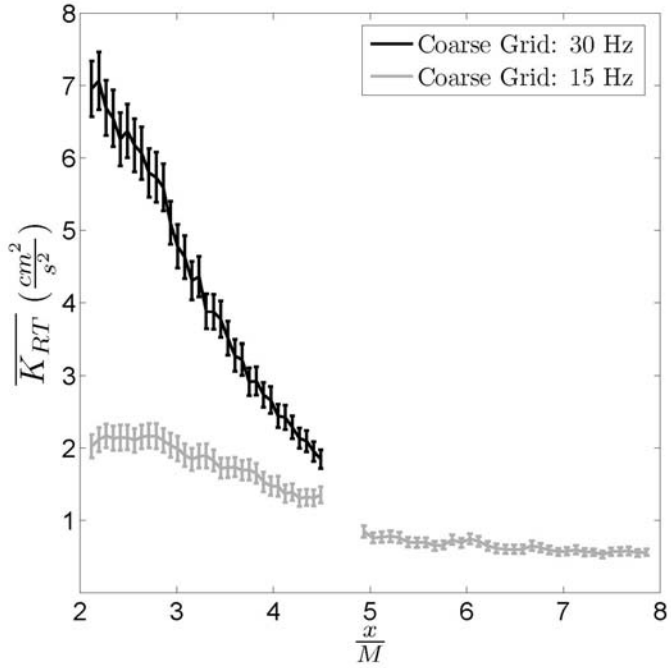

Figure F.2. Downstream evolution of centerline turbulent kinetic energy, with error bars, for the coarse grid experiment processed at 15 and 30 Hz.

APPENDIX G

BHR TURBULENT TRANSPORT MODEL EQUATIONS

The BHR turbulent transport model is derived from Navier-Stokes equations for compressible, variable-density flows of a single material. Typically, single-point turbulence models decompose flow variables into their mean and fluctuating quantities using Reynolds decomposition. However, for variable-density density BHR model, the variables are decomposed into mass-weighted averages (Farve decomposition). An example of the decomposition of the velocity variable using Farve decomposition is seen in Equation (G.1) (Besnard *et al.*, 1992).

$$u_i = \tilde{u}_i + u_i''; \quad \text{where} \quad \tilde{u}_i = \frac{\overline{\rho u_i}}{\bar{\rho}} \tag{G.1}$$

The BHR modeled transport equations for the turbulent kinetic energy, turbulent length scale, the turbulent mass flux, and the species concentration solved by RAGE are given in Equations (G.2-5) (Steinkamp *et al.*, 2001).

$$\frac{\partial \bar{\rho} K}{\partial t} + \frac{\partial \bar{\rho} K \tilde{u}_n}{\partial x_n} = a_n \frac{\partial \bar{p}}{\partial x_n} - R_{in} \frac{\partial \tilde{u}_i}{\partial x_n} + \frac{\partial}{\partial x_n}\left(\bar{\rho} \upsilon_t \frac{\partial K}{\partial x_n}\right) - \bar{\rho} \frac{K^{3/2}}{S} \tag{G.2}$$

$$\begin{aligned} \frac{\partial \bar{\rho} S}{\partial t} + \frac{\partial \bar{\rho} S \tilde{u}_n}{\partial x_n} = \frac{S}{K}\left[\left(\frac{3}{2} - C_4\right) a_n \frac{\partial \bar{p}}{\partial x_n} - \left(\frac{3}{2} - C_1\right) R_{in} \frac{\partial \tilde{u}_i}{\partial x_n}\right] - C_3 \bar{\rho} S \frac{\partial \tilde{u}_n}{\partial x_n} \\ + \frac{\partial}{\partial x_n}\left(\frac{\bar{\rho} \nu_t}{\sigma_\varepsilon} \frac{\partial S}{\partial x_n}\right) - \left(\frac{3}{2} - C_2\right) \bar{\rho} \sqrt{k} \end{aligned} \tag{G.3}$$

$$\frac{\partial \bar{\rho} a_i}{\partial t} + \frac{\partial \bar{\rho} a_i \tilde{u}_n}{\partial x_n} = \left(C_{a2} b\right) \frac{\partial \bar{p}}{\partial x_i} - \frac{R_{in}}{\bar{\rho}} \frac{\partial \bar{\rho}}{\partial x_n} - \frac{C_{a1} \bar{\rho} a_i \sqrt{K}}{S} - \bar{\rho} a_n \frac{\partial\left(\tilde{u}_i - a_i\right)}{\partial x_n} \tag{G.4}$$

$$\frac{\partial \bar{\rho} \tilde{c}_\alpha}{\partial t} + \frac{\partial \bar{\rho} \tilde{c}_\alpha \tilde{u}_n}{\partial x_n} = \frac{\partial}{\partial x_n}\left(\frac{\bar{\rho} \nu_t}{\sigma_c} \frac{\partial \tilde{c}_\alpha}{\partial x_n}\right) \tag{G.5}$$

The Reynolds stress tensor, turbulent kinetic energy dissipation rate, turbulent viscosity, and turbulent kinetic energy definitions are given in Equations (G.6-9) (Steinkamp *et al.,* 2001).

$$R_{ij} = -\overline{\rho}\nu_t\left(\frac{\partial \widetilde{u}_i}{\partial x_j} + \frac{\partial \widetilde{u}_j}{\partial x_i}\right) + \frac{2}{3}\delta_{ij}\left(\overline{\rho}\nu_t \frac{\partial \widetilde{u}_n}{\partial x_n} + \overline{\rho}K\right) \tag{G.6}$$

$$\varepsilon = \frac{K^{3/2}}{S} \tag{G.7}$$

$$\nu_t = C_\mu S\sqrt{K} \tag{G.8}$$

$$K = \frac{1}{2\overline{\rho}} R_{nn} \tag{G.9}$$

The hydrodynamic equations solved in the RAGE hydro-code are the mass, momentum, and internal energy equations, seen in Equations (G.10-12) (Gittings *et al.*, 2006).

$$\frac{\partial \rho}{\partial t} + \nabla \cdot (\rho u) = 0 \tag{G.10}$$

$$\frac{\partial (\rho u)}{\partial t} + \nabla \cdot (\rho u u + P) = \rho g \tag{G.11}$$

$$\frac{\partial (\rho E_m)}{\partial t} + \nabla \cdot (\rho E_m u + P \cdot u) = \rho g \cdot u \tag{G.12}$$

Implementing the BHR model equations into RAGE, with *K, S,* and *a* being the transported model variables, the RAGE equations become (Steinkamp *et al.*, 2001):

$$\frac{\partial \overline{\rho} c_\alpha}{\partial t} + \nabla \cdot \left(\overline{\rho} c_\alpha \widetilde{u}\right) = \nabla \cdot \left(\frac{\overline{\rho}\nu_t}{\sigma_c} \nabla c_\alpha\right) \tag{G.13}$$

$$\frac{\partial \overline{\rho}\widetilde{u}}{\partial t} + \nabla \cdot \left(\overline{\rho}\widetilde{u}\widetilde{u}\right) = -\nabla \overline{p} + \nabla \cdot R \tag{G.14}$$

$$\begin{aligned} \frac{\partial \overline{\rho} E}{\partial t} + \nabla \cdot \left(\overline{\rho} E \widetilde{u}\right) = & -\nabla \cdot \left[\overline{p}\left(\widetilde{u} - a\right)\right] - \nabla \cdot \left(\widetilde{u} \cdot R\right) \\ & + \nabla \cdot \overline{\rho}\upsilon_t \left[\nabla K + \frac{C_p}{\sigma_t} \nabla I + \sum_{\alpha=1}^{nmats} h_\alpha c_\alpha\right] \end{aligned} \tag{G.15}$$

where: $$\overline{\rho c}_{\alpha} = \left(\frac{M}{V}\right)\left(\frac{m_{\alpha}}{M}\right) = \frac{m_{\alpha}}{V}; \quad \sum_{\alpha} \frac{m_{\alpha}}{V} = \overline{\rho}$$

The driving force for the growth of the RT instability for the BHR mix model is the amount of turbulent diffusion occurring between the species (defined by Equation (G.5)). The transport of the species concentration can be seen in Equation (G.13) with the implementation of the BHR model into RAGE.

APPENDIX H

UNCERTAINTY ANALYSIS

An uncertainty analysis has been performed on each of the measured parameters of this investigation. Methods described by Kline and McClintock (1953) and Benedict and Gould (1996) are used to determine uncertainties in the turbulent statistics presented.

The equation of state to obtain the density of water is given again in Equation (H.1).

$$\rho(T) = \frac{\begin{pmatrix} 999.8396 + 18.2249T - 0.007922T^2 - 55.448\times10^{-6}T^3 \\ +149.756\times10^{-9}T^4 - 393.295\times10^{-12}T^5 \end{pmatrix}}{1+18.159\times10^{-3}T} \tag{H.1}$$

The uncertainty of the densities from the cold and warm streams is determined using Equation (H.2).

$$\omega_\rho = \left[\left(\frac{\partial\rho(T)}{\partial T}\omega_T \right)^2 \right]^{1/2} \tag{H.2}$$

The density uncertainties of the warm and cold water are used to obtain the uncertainty of the Atwood number using Equation (H.3).

$$\omega_{A_t} = \left[\left(\frac{\partial A_t}{\partial \rho_l}\omega_{\rho_l} \right)^2 + \left(\frac{\partial A_t}{\partial \rho_h}\omega_{\rho_h} \right)^2 \right]^{1/2} \tag{H.3}$$

Incorporating the uncertainty of the uncertainty of the Atwood number the uncertainty of the growth parameter, α, (defined as $\alpha = h/A_t g\, t^2$) is measured using Equation (H.4).

$$\omega_\alpha = \left[\left(\frac{\partial\alpha}{\partial h}\omega_h \right)^2 + \left(\frac{\partial\alpha}{\partial A_t}\omega_{A_t} \right)^2 + \left(\frac{\partial\alpha}{\partial g}\omega_g \right)^2 + \left(\frac{\partial\alpha}{\partial t}\omega_t \right)^2 \right]^{1/2} \tag{H.4}$$

Several turbulence statistics are necessary to evaluate quantities of interest. Benedict and Gould present an uncertainty analysis that provides a non-Gaussian approach to the estimation of the

uncertainty of turbulence measurements (Benedict & Gould 1996). Turbulence quantities of interest for the present study include the vertical and stream-wise velocity fluctuations, $\sqrt{\overline{u'^2}}$ and $\sqrt{\overline{v'^2}}$, and the vertical and stream-wise velocity variances, $\overline{u'^2}$ and $\overline{v'^2}$. Example uncertainties given by Benedict & Gould for the stream-wise velocity fluctuations and variances are given in Equations (H.5-6), where *N* is the number of independent samples (Benedict & Gould 1996).

$$\frac{\left(\overline{u^4} - \left(\overline{u^2}\right)^2\right) / 4\overline{u^2}}{N} \tag{H.5}$$

$$\frac{\overline{u^4} - \left(\overline{u^2}\right)^2}{N} \tag{H.6}$$

Using the variances given in Equations (H.5-6), the 5-95% confidence interval is available for the determination of uncertainty in the turbulent kinetic energy of the centerline, $\overline{K_{RT}}$, and outside the mixing layer, $\overline{K_{GT}}$, and are given in Equations (H.7-8).

$$\omega_{\overline{K_{RT}}} = \left[\left(\frac{\partial \overline{K_{RT}}}{\partial \overline{u'^2}} \omega_{\overline{u'^2}} \right)^2 + \left(\frac{\partial \overline{K_{RT}}}{\partial \overline{v'^2}} \omega_{\overline{v'^2}} \right)^2 \right]^{1/2} \tag{H.7}$$

$$\omega_{\overline{K_{GT}}} = \left[\left(\frac{\partial \overline{K_{GT}}}{\partial \overline{u'^2}} \omega_{\overline{u'^2}} \right)^2 + \left(\frac{\partial \overline{K_{GT}}}{\partial \overline{v'^2}} \omega_{\overline{v'^2}} \right)^2 \right]^{1/2} \tag{H.8}$$

The uncertainty of the least squares fit for the isotropic decay exponent, *n*, and coefficient, *A*, were determined by performing a "worst fit" on the data using the uncertainty of the dependent variable. Using the uncertainty of the isotropic decay exponent, *n,* the uncertainty of the isotropic decay constant for the model, *C2*, is evaluated using Equation (H.9).

$$\omega_{C2} = \left[\left(\frac{\partial C2}{\partial n} \omega_n \right)^2 \right]^{1/2} \tag{H.9}$$

The uncertainty of the dissipation, ε, is found using Equation (H.10), using the uncertainty of the turbulent kinetic energy.

$$\omega_{\varepsilon} = \left[\left(\frac{\partial \varepsilon}{\partial \overline{K_{GT}}} \omega_{\overline{K_{GT}}} \right)^2 + \left(\frac{\partial \varepsilon}{\partial t} \omega_t \right)^2 \right]^{1/2} \tag{H.10}$$

The uncertainty of the turbulent length scale, $\overline{S}$, is found using Equation (H.11) with the uncertainties of the turbulent kinetic energy of the free stream and the dissipation term.

$$\omega_{\overline{S}} = \left[\left(\frac{\partial \overline{S}}{\partial \overline{K_{GT}}} \omega_{\overline{K_{GT}}} \right)^2 + \left(\frac{\partial \overline{S}}{\partial \varepsilon} \omega_{\varepsilon} \right)^2 \right]^{1/2} \tag{H.11}$$

The uncertainty of the growth parameter for the turbulent kinetic energy, α_K, is determined using the uncertainty of the centerline turbulent kinetic energy, $\overline{K_{RT}}$, to obtain a "worst fit" line.

A summary of the representative uncertainties of the measurements obtained for this investigation are given in Table H.1.

Parameter	% Uncertainty
U_m	5
$\overline{u'^2}$	12
$\overline{v'^2}$	11
$\sqrt{\overline{u'^2}}$	6
$\sqrt{\overline{v'^2}}$	5
A_t	1
$\overline{K_{RT}}$	12
$\overline{K_{GT}}$	10
n	10
ε	5
$\overline{S}$	15
α	5
α_K	54

Table H.1. Estimated uncertainties of experimentally measured parameters.

VITA

Name:	Freeman Michael Peart
Permenant Residence:	495 Jones Street Bridge City, Texas 77611
Education:	B.S. (Mechanical Engineering), May 2006 Texas A&M University, College Station, Texas
	M.S. (Mechanical Engineering), August 2008 Texas A&M University, College Station, Texas